

FAST Adaptive Smoothing and Thresholding for Improved Activation Detection in Low-Signal fMRI

Israel Almodóvar-Rivera and Ranjan Maitra

Abstract

Functional Magnetic Resonance Imaging is a noninvasive tool used to study brain function. Detecting activation is challenged by many factors, and even more so in low-signal scenarios that arise in the performance of high-level cognitive tasks. We provide a fully automated and fast adaptive smoothing and thresholding (FAST) algorithm that uses smoothing and extreme value theory on correlated statistical parametric maps for thresholding. Performance on experiments spanning a range of low-signal settings is very encouraging. The methodology also performs well in a study to identify the cerebral regions that perceive only-auditory-reliable and only-visual-reliable speech stimuli as well as those that perceive one but not the other.

Index Terms

AM-FAST, AR-FAST, Adaptive Segmentation, AFNI, BIC, CNR, Cluster Thresholding, SPM, SUMA, TFCE

I. INTRODUCTION

FUNCTIONAL Magnetic Resonance Imaging (fMRI) [1]–[9] studies the spatial characteristics and extent of brain function while at rest or, more commonly, while performing tasks or responding to external stimuli. In the latter scenario, which is the setting for this paper, the imaging modality acquires voxel-wise Blood-Oxygen-Level-Dependent (BOLD) measurements [10], [11] at rest and during stimulation or performance of a task. After pre-processing, a statistical model such as a general linear model [4], [12] is fit to the time course sequence against the expected BOLD response [13]–[15]. Statistical Parametric Mapping (SPM) [16] techniques provide voxel-wise test statistics summarizing the association between the time series response at that voxel and the expected BOLD response [3]. The map of test statistics is then thresholded to identify significantly activated voxels [17]–[19]. The analysis of fMRI datasets is challenged [20]–[23] by factors such as scanner, inter- and intra-subject variability, voluntary/involuntary or stimulus-correlated motion and also the several-seconds delay in the BOLD response while the neural stimulus passes through the hemodynamic filter [23]–[25]. Pre-processing steps [22], [26] mitigate some of these effects, but additional challenges are presented by the fact that an fMRI study is expected to have no more than 1-3% activated voxels [8], [27]. Also, many activation studies involving high-level cognitive processes have low contrast-to-noise ratios (CNR), throwing up more issues as illustrated next.

A. Activation Detection during Noisy Audiovisual Speech

The most important form of human communication is speech [28]–[30], which the brain is adept at understanding even in noisy surroundings. This ability may be due [31] to the brain’s capacity for multisensory integration of independently-acquired visual and auditory input information which reduces noise and allows for more accurate perception [32], [33]. Recently, [31] studied the role of the superior temporal sulcus (STS) in perceiving noisy speech, through fMRI and behavioral experiments, and established increased connectivity between the STS and the auditory or the visual cortex depending on whichever modality was more reliable, that is, less noisy.

[31] provided results on regions of interest (ROIs) drawn on the STS and the auditory and visual cortices. However, the full benefit of fMRI can be realized only if we move beyond assessing cerebral function at the ROI level to understanding it at the voxel level. Reliable voxel-wise activation detection in individual subjects may also allow for the further adoption of fMRI in a clinical setting. All these are potential scenarios with low CNRs where accurate activation detection methods are needed. We return to this application in Section IV.

I. Almodóvar-Rivera is with the Department of Biostatistics and Epidemiology at the University of Puerto Rico, Medical Science Campus, San Juan, Puerto Rico, USA.

R.Maitra is with the Department of Statistics, Iowa State University, Ames, Iowa, USA.

An earlier version of this article won I. Almodóvar-Rivera a Student Paper Competition award sponsored by the American Statistical Association Section on Medical Devices and Diagnostics at the 2018 Joint Statistical Meetings.

This research was supported in part by the National Institute of Biomedical Imaging and Bioengineering (NIBIB) of the National Institutes of Health (NIH) under its Award No. R21EB016212. I. Almodóvar-Rivera also acknowledges receipt of a fellowship from Iowa State University’s Alliance for Graduate Education and the Professoriate (AGEP) program for underrepresented graduate students in STEM fields. The content of this paper however is solely the responsibility of the authors and does not represent the official views of either the NIBIB or the NIH.

©2017 IEEE. Personal use of this material is permitted. However, permission to use this material for any other purposes must be obtained from the IEEE by sending a request to pubs-permissions@ieee.org.

Manuscript received xxxx xx, 201x; revised xxxxxxxx xx, 201x. Accepted xxxxxxxx xx, 201x. First published xxxxxxxx x, xxxx, current version published yyyyymm d, yyyy.

Color versions of one or more of the figures in this paper are available online at <http://ieeexplore.org>.

Digital Object Identifier

B. Background and Current Practices

Many thresholding methods [34]–[39] in fMRI address multiple testing issues in determining significance of test statistics but ignore spatial resolution. Acquired images are instead often spatially smoothed prior to analysis, but such non-adaptive smoothing reduces both the adaptive spatial resolution and the number of available independent tests for activation detection [40]. Iterative adaptive smoothing and segmentation methods in the form of propagation-separation (PS) [40] and adaptive-segmentation (AS) [41] have been developed. While operationally different, both methods essentially segment the SPM into activated and inactivated voxels. PS approximately yields a random t -field and uses Random Field Theory for segmentation while AS uses multi-scale testing. [41] argued for AS, because of its more general development and fewer model assumptions. AS also requires no heuristic corrections for spatial correlation, provides decisions at prescribed significance levels and showed better performance over PS in an auditory experiment [41]. However, AS requires pre-specified bandwidth sequences and ignores correlation within the SPM. So Section II of this paper develops theory and methodology for a fully automated Fast Adaptive Smoothing and Thresholding (FAST) algorithm that accounts for correlation and obviates the need for setting any parameter beyond the significance level. FAST's performance is evaluated in Section III on real datasets and large-scale simulation experiments. Section IV applies FAST to the dataset of Section I-A. The paper ends with some discussion. We also have an online supplement with additional illustrations that are referenced with the prefix “S”.

II. THEORY AND METHODS

A. Preliminaries

Let \mathbf{Y}_i be the time series vector of the observed BOLD response at the i th voxel obtained after preprocessing for registration and motion correction. It is common to relate \mathbf{Y}_i to the expected BOLD response via the general linear model

$$\mathbf{Y}_i = \mathbf{X}\boldsymbol{\beta}_i + \boldsymbol{\epsilon}_i, \quad (1)$$

where $\boldsymbol{\epsilon}_i$ is a p th-order auto-regressive (AR) Gaussian error vector with AR coefficients $\boldsymbol{\phi}_i = (\phi_{i1}, \phi_{i2}, \dots, \phi_{ip})$ and marginal variance σ_i^2 . Without loss of generality (w.l.o.g.), assume that the design matrix \mathbf{X} has the intercept in the first column, the expected BOLD response for the k stimulus levels in the next k columns, and polynomial terms for the drift parameter in the remaining m columns. Therefore, $\boldsymbol{\beta}$ is a coefficient vector of length $d = k + m + 1$. We assume that the image volume has n voxels: thus $i = 1, 2, \dots, n$ in (1). The parameters $(\hat{\boldsymbol{\beta}}_i, \hat{\sigma}_i^2, \hat{\boldsymbol{\phi}}_i)$ s are usually estimated via generalized least squares or restricted maximum likelihood. A typical analysis approach then applies (voxel-wise) hypothesis tests with the null hypothesis specifying no activation owing to the stimulus or task. SPMs of the form $\boldsymbol{\Gamma} = \{c'\hat{\boldsymbol{\beta}}_i\}_{i \in V}$ with appropriate contrasts $c'\hat{\boldsymbol{\beta}}_i$ are then formulated at each voxel.

Many researchers use models that assume independence or AR(1) errors: others pre-whiten the time series before fitting (1) under independence. Incorrect model specifications can yield less precise SPMs [42]–[45]. In this paper, we assumed AR(p) errors, with p assessed via the Bayes Information Criterion (BIC) [46], [47] that measures a fitted model's quality by trading its complexity against its fidelity to the data. Tests on the SPM $\boldsymbol{\Gamma}$ identify voxels that are activated with the stimulus. Specifically, voxel $i \in V$ is declared as activated if a suitable test rejects the hypothesis of null activation. Our objective is to develop an approach that adaptively and automatically smooths and thresholds the SPM while accounting for spatial correlation and the fact that these sequence of thresholds yield SPMs from truncated distributions. Before detailing our algorithm, we provide some theoretical development.

B. Theoretical Development

We assume t -distributed SPMs with degrees of freedom large enough for the SPM to be approximately standard normally distributed under the null hypothesis of no activation. We also assume a homogeneous correlation structure for the SPM, which is reasonable given our use of a radially symmetric kernel for smoothing. We have

Theorem 1. *Let $\mathbf{X} \sim N_n(\mathbf{0}, \mathbf{R})$ where $\mathbf{X} = (X_1, \dots, X_n)'$ and \mathbf{R} is a circulant correlation matrix. Writing $\mathbf{1} = (1, 1, \dots, 1)'$, we let $\rho = \mathbf{R}^{-\frac{1}{2}}\mathbf{1}$ be the sum of the elements in the first row of $\mathbf{R}^{-\frac{1}{2}}$. Further, let $X_{(n)}$ be the maximum value of \mathbf{X} , that is, $X_{(n)} = \max\{X_1, X_2, \dots, X_n\}$. Then the cumulative distribution function (c.d.f.) $F_n(x)$ of $X_{(n)}$ is given by $F_n(x) = P(X_{(n)} \leq x) = [\Phi(\rho x)]^n$, where $\Phi(\cdot)$ is the c.d.f. of the standard normal random variable.*

Proof. From the definition of $X_{(n)}$, we have

$$\begin{aligned} F_n(x) &= P(\mathbf{X} \leq x\mathbf{1}) \\ &= P(\mathbf{R}^{-1/2}\mathbf{X} \leq x\mathbf{R}^{-1/2}\mathbf{1}) \\ &= P(\mathbf{Y} \leq \rho x\mathbf{1}), \text{ where } \mathbf{Y} \sim N_n(\mathbf{0}, \mathbf{I}_n) \\ &= P(Y_i \leq \rho x, \quad \forall i = 1, 2, \dots, n) = [\Phi(\rho x)]^n. \end{aligned} \quad (2)$$

□

In the limit, we are led to the following

Corollary 2. *Let \mathbf{X} and $X_{(n)}$ be as in Theorem 1. Then the limiting distribution of $X_{(n)}$ belongs to the domain of attraction of the Gumbel distribution, and satisfies:*

$$\lim_{n \rightarrow \infty} [F_n(a_n x + b_n)] = \exp\{e^{-x}\}, \quad (3)$$

where $a_n = \rho/[n\phi(b_n)]$ and $b_n = \Phi^{-1}(1 - 1/n)\rho$, with $\phi(\cdot)$ being the standard normal probability density function (p.d.f.).

Proof. For $\mathbf{Y} \sim N_n(\mathbf{0}, \mathbf{I}_n)$, the limiting distribution of $Y_{(n)}$ satisfies $\lim_{n \rightarrow \infty} [\Phi(a_n x + b_n)]^n = \exp\{e^{-x}\}$, with $a_n = 1/[n\phi(b_n)]$ and $b_n = \Phi^{-1}(1 - 1/n)$ [48]. The result follows from Theorem 1. \square

Theorem 1 and Corollary 2 provide the wherewithal for choosing a threshold using the limiting distribution of the maximum of correlated normal random variables with circulant correlation structure. Note however, that the first thresholding step results in *truncated* (and correlated) random variables that are under consideration for thresholding in subsequent steps. We account for this added complication by deriving the limiting distribution of the maximum of a correlated sample from a right-truncated normal distribution. We do so by first noting that if Y_1, Y_2, \dots, Y_n are independent identically distributed random variables from the standard normal p.d.f truncated at η , then each Y_i has p.d.f. $\phi_\eta^\bullet(\cdot)$ and c.d.f. $\Phi_\eta^\bullet(\cdot)$:

$$\phi_\eta^\bullet(x) = \frac{\phi(x)}{\Phi(\eta)} I(x < \eta); \quad \Phi_\eta^\bullet(x) = \frac{\Phi(x)}{\Phi(\eta)} I(x < \eta). \quad (4)$$

where $I(\cdot)$ is 1 if $x < \eta$ and 0 otherwise. Then $Y_{(n)} = \max\{Y_i, i = 1, 2, \dots, n\}$ has c.d.f. $G_\eta^\bullet(x) = [\Phi(x)/\Phi(\eta)]^n I(x < \eta)$ with limiting distribution given by Theorem 3.

Theorem 3. *Let Y_1, Y_2, \dots, Y_n be a sample from (4). Then the limiting distribution of $Y_{(n)}$ belongs to the domain of attraction of the reverse Weibull distribution and satisfies*

$$\lim_{n \rightarrow \infty} [G_\eta^\bullet(a_n^\bullet x + b_n^\bullet)] = \exp\{-(-x^{-\tau})\} I(x \leq 0). \quad (5)$$

for some $\tau > 0$. Here $a_n^\bullet = \eta - \Phi_\eta^\bullet - 1(1 - 1/n)$ and $b_n^\bullet = 0$.

Proof. Note that $\eta = \sup\{x \mid \Phi_\eta^\bullet(x) < 1\}$. From Theorem 10.5.2 in [49], a sufficient condition for $Y_{(n)}$ to be the domain of attraction is to demonstrate that

$$\lim_{x \rightarrow \eta} \frac{(\eta - x)\phi_\eta^\bullet(x)}{1 - \Phi_\eta^\bullet(x)} = \tau$$

for some $\tau > 0$ [50]. In our case, the limit holds because $\eta < \infty$. Then, using L'Hôpital's rule, we have

$$\begin{aligned} \lim_{x \rightarrow \eta} \frac{(\eta - x)\phi_\eta^\bullet(x)}{1 - \Phi_\eta^\bullet(x)} &= \lim_{x \rightarrow \eta} \frac{(\eta - x) \frac{d}{dx} \phi_\eta^\bullet(x) - \phi_\eta^\bullet(x)}{-\phi_\eta^\bullet(x)} \\ &= \lim_{x \rightarrow \eta} \frac{(\eta - x)\phi'_\eta(x)/\Phi(\eta) - \phi(x)/\Phi(\eta)}{-\phi(x)/\Phi(\eta)} \\ &= 1 \end{aligned}$$

Thus the right-truncated normal distribution satisfies the reverse Weibull condition and converges to the reverse Weibull distribution with $\tau \equiv 1$ in (5). The constants in the theorem are as per extreme value theory [48], [49]. \square

Theorem 4. *Let \mathbf{X} be a random vector from the $N_n(\mathbf{0}, \mathbf{R})$ density but that is right-truncated in each coordinate at η , with \mathbf{R} being a circulant correlation matrix. Let $\rho = \mathbf{R}^{-\frac{1}{2}}\mathbf{1}$ be the sum of the elements in the first row of $\mathbf{R}^{-\frac{1}{2}}$. Also, let $X_{(n)}$ be defined as before. Then the c.d.f. $F_\eta^\bullet(x)$ of $X_{(n)}$ is given by $F_\eta^\bullet(x) = P(X_{(n)} \leq x) = [\Phi(\rho x)/\Phi(\eta)]^n I(x < \eta)$.*

Proof. Proceeding as in the proof of Theorem 1 yields

$$\begin{aligned} F_\eta^\bullet(x) &= P(\mathbf{X} \leq x\mathbf{1}) \\ &= P(\mathbf{R}^{-1/2}\mathbf{X} \leq x\mathbf{R}^{-1/2}\mathbf{1}) \\ &= P(\mathbf{Y} \leq \rho x\mathbf{1}), \text{ where } Y_i \text{ s are i.i.d. } \Phi_{\rho\eta}^\bullet(y) \\ &= G_{\rho\eta}^\bullet(\rho x) = [\Phi(\rho x)/\Phi(\eta)]^n I(x < \eta). \end{aligned} \quad (6)$$

\square

Corollary 5. *Let \mathbf{X} and $X_{(n)}$ be as in Theorem 4. Then the limiting distribution of $X_{(n)}$ belongs to the domain of attraction of the reverse Weibull distribution, and satisfies:*

$$\lim_{n \rightarrow \infty} [F_\eta^\bullet(a_n^\bullet x + b_n^\bullet)] = \exp\{-(-x^{-\alpha})\} I(x \leq 0). \quad (7)$$

where $a_n^\bullet = (\eta - \Phi_{\rho\eta}^\bullet - 1(1 - 1/n))\rho$ and $b_n^\bullet = 0$.

Proof. From Theorem 3, the limiting distribution of $Y_{(n)}$ is (5) so $F_\eta^\bullet(x) = G_{\rho\eta}^\bullet(\rho x)$ in Theorem 4. The result follows. \square

C. Fast Adaptive Smoothing and Thresholding

We now propose our FAST algorithm that adaptively and, in sequence, smooths and identifies activated regions by thresholding. We estimate the amount of smoothing robustly or from the correlation structure, which we assume is well-approximated by a 3D Gaussian kernel. Thus, under the null hypothesis (of no activation anywhere), we assume that the SPM $\Gamma \sim N(\mathbf{0}, \mathbf{R})$ where $\mathbf{R} = \mathbf{S}_h$ with h the smoothing parameter of \mathbf{S}_h given in terms of its full-width-at-half-maximum. Let $\Gamma_{(-h)} \sim \mathbf{S}_h^{-\frac{1}{2}} \Gamma$. Then estimate h by maximizing the loglikelihood function

$$\ell(h \mid \Gamma_{(-h)}) = -\frac{n}{2} \log(2\pi) - \frac{1}{2} \log |\mathbf{S}_h| - \frac{1}{2} \mathbf{\Gamma}'_{(-h)} \mathbf{\Gamma}_{(-h)}. \quad (8)$$

Note that $\Gamma_{(-h)}$ and $|\mathbf{S}_h|$ are speedily computed using Fast Fourier Transforms (FFTs). Starting with the SPM Γ , obtained as discussed in Section II-A, we propose the algorithm:

- 1) *Initial Setup.* At this point, assume that $\zeta_i \equiv 0 \forall i$, where ζ_i is the activation status of the i th voxel. That is, assume that all voxels are inactive. Set $\zeta_i^{(0)} \equiv \zeta_i$. Also denote $\mathbf{\Gamma}_{(0)} = \mathbf{\Gamma}$, and $n_0 = n$, where n_k denotes the number of voxels for which $\zeta_i^{(k)} = 0$.
- 2) *Iterative Steps.* For $k = 1, 2, \dots$, iterate as follows:
 - a) *Smoothing.* We smooth $\mathbf{\Gamma}_{(k-1)}$ in one of two ways:
 - i) *Adaptive Maximum Likelihood (AM-FAST, pronounced ām-fast):* Maximize (8) given $\mathbf{\Gamma}_{(k-1)}$ to obtain h_k . Obtain $\Gamma_{(k)}$ by smoothing $\mathbf{\Gamma}_{(k-1)}$ with \mathbf{S}_{h_k} . Also obtain $\rho_k = \mathbf{S}_{h_k}^{-\frac{1}{2}} \mathbf{1}$.
 - ii) *Adaptive Robust Smoothing (AR-FAST, pronounced ahr-fast):* Use robust methods [51] on $\mathbf{\Gamma}_{(k-1)}$ to get $\mathbf{\Gamma}_{(k)}$. Now, maximize (8) given $\mathbf{\Gamma}_{(k)}$ to obtain h_k and $\rho_k = \mathbf{S}_{h_k}^{-\frac{1}{2}} \mathbf{1}$.
 - b) *Adaptive Thresholding.* This consists of two steps:
 - i) For $k = 1$, use Corollary 2 to obtain a_n and b_n , otherwise (i.e. for $k > 1$) use Corollary 5 to obtain $a_{n_{k-1}}^*$. In both cases, we use the spatial correlation estimated by $\mathbf{S}_{h_{k-1}}$.
 - ii) From the Gumbel (for $k = 1$) or reverse Weibull distributions (for $k > 1$), get

$$\eta_k = \begin{cases} a_{n_0} \iota_\alpha^G + b_{n_0} & \text{for } k = 1 \\ a_{n_{k-1}}^* \iota_\alpha^W & \text{otherwise.} \end{cases} \quad (9)$$

where ι_α^G and ι_α^W are the upper-tail α -values for the Gumbel and the reverse Weibull (with $\tau = 1$) distributions, respectively.

- iii) Set all $\zeta_i^{(k)} = 1$ if $\zeta_i^{(k-1)} = 0$ and if the i th coordinate of $\mathbf{\Gamma}_{(k)}$ exceeds η_k . Also, update $n_k = \sum_{i=1}^n \zeta_i^{(k)}$.
- 3) *Termination.* Let $J(\zeta^{(k)}, \zeta^{(k-1)})$ be the Jaccard Index [52], [53] of the activation maps in the k th and $(k-1)$ th iterations. If $J(\zeta^{(k)}, \zeta^{(k-1)}) \leq J(\zeta^{(k+1)}, \zeta^{(k)})$, the algorithm terminates – the final activation map is $\zeta^{(k)}$.

Comments: A few comments are in order:

a) *Correlation structure:* A circulant correlation structure allows for spatial context in the association between the values of the voxel-wise test statistics, while having the added benefit of speedy computations via the use of FFTs.

b) *Comparison with AS:* AS [41] also provides an adaptive weighted smoothing approach based on multi-scale testing. Both AM-FAST and AR-FAST have similarities with AS, in that they also smooth and threshold iteratively. However, there are a few fundamental differences. For one, the AS approach has a set user-specified sequence of bandwidths that smooths $\Gamma_{(k)}$ at each step. In contrast, we use likelihood maximization (for AM-FAST) or robust (for AR-FAST) methods to optimally determine h at each step. AS also performs thresholding in a similar manner as us, but they use a general Fréchet extreme value distribution. Their development ignores both the spatial context and also the fact that thresholding results in subsequent truncated decisions. Our development represents the procedure more accurately because we account for both the correlation structure (resulting in the initial cut-off decided as per the Gumbel distribution) and the truncation (with the subsequent cut-offs being determined by the reverse Weibull distribution). Finally, our method is completely data-driven, with termination declared only when the Jaccard index indicates no substantial changes in the detected activation.

c) *Thresholding:* A reviewer wondered about multiple comparisons because of the connection of hypothesis testing with thresholding. Our cutoff at each iteration depends on the conditional distribution given prior thresholding. Therefore, for I iterations, the overall significance is α^I which is not more than α . We study the role of α in the next section.

d) *Two-sided alternatives:* Our development here builds from one-sided tests where large values are the extreme values of the SPM. For two-sided alternatives, we suggest using the algorithm individually on the SPM and its negative, but using $\alpha/2$ in place of α in (9). This provides two (disjoint) activation maps, the union of which is the two-sided activation map.

III. PERFORMANCE EVALUATIONS

We studied performance of FAST relative to some of the most popular and relevant ones. Our evaluations were on real and simulated datasets and compared FAST with cluster thresholding (CT) applied with $\alpha = 0.001$ per [39], a second-order



Fig. 1: The summarized Jaccard index ($\tilde{\omega}$) of activations obtained by each method over the replications for the RH and LH experiments. In this and other figures, AR- F_a and AM- F_a denote AM-FAST and AR-FAST methods with $\alpha = a$.

neighborhood and number of voxels in cluster determined by [54]’s `3dClustSim` function, threshold-free cluster enhancement (TFCE) [38], permutation-based testing (PBT) [55], AS and PS (applied as AWS or adaptive-weighted smoothing [56]). We used $\alpha = 0.01$ and $\alpha = 0.05$ in FAST to obtain insight into the role of α . We used R packages `RFASTfMRI` for FAST, `FMRI` for AS and AWS, `ANALYZEFMRI` for CT and `PERMUCO` for TFCE and PBT.

A. Finger-Tapping Experiments

Our first set of evaluations used the 12 replicated SPMs [24], [57] from the right-hand (RH) and left-hand (LH) finger tapping study of a RH-dominant male. For each method, Figure 1 indexes the similarity across replications in the activation maps in terms of the summarized Jaccard index ($\tilde{\omega}$). (Pairwise Jaccard indices (ω) between the FAST-obtained activation maps are in Figure S1.) The FAST methods show greater reliability of detected activation than the competitors. There is not much distinction in performance between the FAST methods or α for LH, but RH experiments show AM- and AR-FAST at $\alpha = 0.05$ as the top two performers with TFCE marginally behind and AS and AWS also doing reasonably. Notwithstanding FAST’s relatively superior performance, $\tilde{\omega}$ is generally low and points to potential issues in data quality and processing [53].

B. Experiments on Simulated Phantom Data

Our next set of examples are on simulated phantom data. In each case, data were simulated from (1) and performance evaluated and studied in detail. We discuss performance with the different phantom and experimental conditions next.

1) *Motif and Stripes*: We first study performance on the simulation setup of [41]. We thank K. Tabelow for readily sharing code that created the motif and three striped (16×16 , 32×32 , 64×64) phantoms of Figures 2(a)-(d). The last three examples are of two-sided alternatives. The β s are as in [41]. Our CNRs ranged from 0.75 to 2.68 for the motif and were 1 or 2 for the stripes. All simulations had AR(1) errors with $\rho = 0.3$. For AS and AWS, we adopted the maximum bandwidth sequence values ($h_k^* = 3.06, 1, 2$ and 3) in [41] for the four respective phantoms as the best-case specific choices. Figure 2(e) summarizes

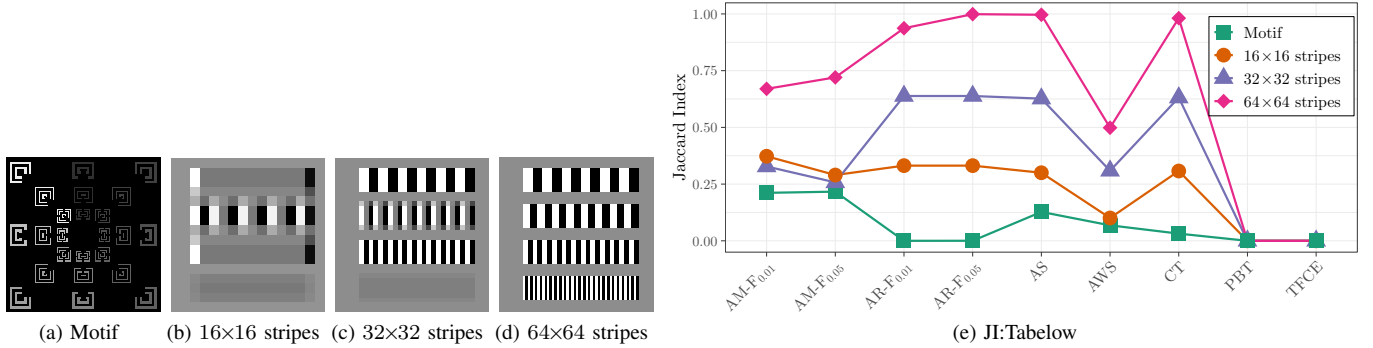


Fig. 2: (a)-(d) The phantoms from [41] and (e) performance of the methods under different settings.

performance. AM-FAST is the best performer on the motif, though all methods perform poorly (Figure S2). AR-FAST, AS and CT are the best performers for the stripes while AM-FAST and AWS perform modestly and PBT and TFCE are failures on these simulations.

2) *Large-scale study with modified Hoffman phantom:* The phantoms in [41], with uniform underlying structure (β_0) and no drift, but varying CNR, are not particularly representative of cerebral activation and so do not provide much insight into performance of different activation methods. So we performed a large simulation study using a more realistic phantom and experimental setup that matches (1). We used a modified version of the digitized 128×128 2D Hoffman phantom [58] of Positron Emission Tomography, with 3465 in-brain pixels, representing two types (say, A and B) of anatomic structures – the latter has 138 deemed truly activated pixels in two distinct regions (Figure 3). The i th pixel in the phantom had values

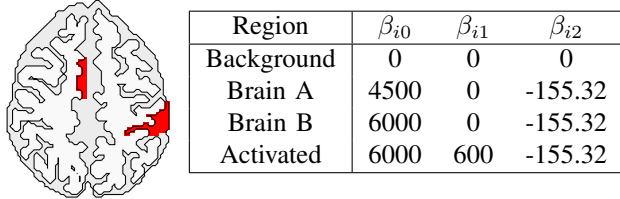


Fig. 3: The modified Hoffman phantom. Putative anatomic regions (A and B) are in shades of grey, with truly activated pixels in red. The table lists the β_i s used in our simulations.

$$\beta_i = (\beta_{i0}, \beta_{i1}, \beta_{i2})$$
 in (1) as per its location (see Figure 3).

As in (1), the design matrix \mathbf{X} had the intercept in the first column. The second column had the hemodynamic response function (HRF) [7] convolved with the input stimulus time series which alternated as 16 on-off blocks of 6 time-points each. The “on” block signaled rest, with input stimulus 0, while the “off” block was 1 to signify activation. The third column of \mathbf{X} represented linear drift and was set to t ($t=1, 2, \dots, 96$). As per (1), AR(p) Gaussian errors were simulated for different p and at each pixel. Specifically, for each p , we considered AR coefficients for a range of $\phi \equiv \phi_i$ s with coefficients $(\phi_1, \phi_2, \dots, \phi_p)$ that were, with lag, (a) all equal, (b) decreasing, (c) increasing, (d) first decreasing and then increasing and (e) first increasing and then decreasing. We restricted $\sum_{j=1}^p \phi_j = 0.9$ to ensure stationary solutions. Thus, for AR(1), we have $\phi_1 \equiv 0.9$ for all cases. For $p=2, 3, 4$, we have $\phi_i \equiv 0.9/p$ for the equal AR coefficients scenario. Table I displays the ϕ -values for the other cases. Finally, σ_0 was chosen to correspond to very low to moderate CNR settings. Specifically, we set $\sigma_0 = 1200, 800, 600$ yielding

TABLE I: ϕ s for the AR(p) scenarios used in our simulations.

p	Decreasing	Increasing
2	(0.6, 0.3)	(0.3, 0.6)
3	(0.4, 0.3, 0.2)	(0.2, 0.3, 0.4)
4	(0.3, 0.25, 0.20, 0.15)	(0.15, 0.20, 0.25, 0.3)
5	(0.3, 0.25, 0.20, 0.10, 0.05)	(0.05, 0.10, 0.20, 0.25, 0.30)

p	Decreasing-Increasing	Increasing-Decreasing
2	(0.6, 0.3)	(0.3, 0.6)
3	(0.4, 0.1, 0.4)	(0.1, 0.7, 0.1)
4	(0.4, 0.05, 0.05, 0.4)	(0.05, 0.4, 0.4, 0.05)
5	(0.25, 0.15, 0.1, 0.15, 0.25)	(0.1, 0.15, 0.4, 0.15, 0.1)

CNR = 0.50, 0.75, and 1.0. By design, our SNRs were 10 times our CNRs. We simulated realizations of time series images using (1) and the setup of Figure 3 and the AR structures in Table I.

For each pixel, (1) was fit with different AR(p), $p = 0, 1, 2, 3, 4, 5$, with the highest BIC used to choose \hat{p} . SPMs were generated as per Section II-A. Figure 4 provides sample SPMs and activation maps with the three top-performing methods: AR-FAST, AM-FAST and AS, for the three CNR settings with AR(2) errors and coefficients decreasing with order. (See Figures S3 for activation maps using all methods and Figures S3–S6 for cases with other p and/or decreasing order.) AS does fairly well only for CNR=1.0 while AM-FAST and AR-FAST identify activation very well at all settings but also identify a few false positives at low CNR. Other methods – in particular CT, TFCE and PBT – barely find activation.

To more fully understand performance, we replicated our experiment 25 times for each simulation setting. Figure S7 shows performance in estimating p , with over-estimation and mild under-estimation for large and small values of true AR order, respectively. The pattern broadly holds for all CNR values and types of ϕ s. We now discuss performance of the activation detection methods on SPMs obtained upon fitting AR(\hat{p}). Figure 5 displays overall performance, in terms of ω , of all methods for the case of ϕ s decreasing with order. Similar results hold for other types of ϕ s (Figure S8). Figures S9–S11 display the number of activated voxels and the false and true positive rates (FPRs and TPRs). These results show FAST as the best performers at all CNRs, with AR-FAST near-perfect for experiments with higher AR orders. AS and AWS, in that order, are the better performers among the competitors but CT, TFCE and PBT perform very poorly with very low TPRs (of below 25%). The FAST methods have very high TPRs but FPRs of up to 0.35% and 0.45% for AM- and AR-FAST for $\alpha = 0.05$ and in cases with low CNR and p – these FPRs decrease with increasing CNR. Overall, the slightly higher FPR of the FAST methods is overwhelmed by the vastly higher TPR, resulting in theirs being the best performers (as per ω).

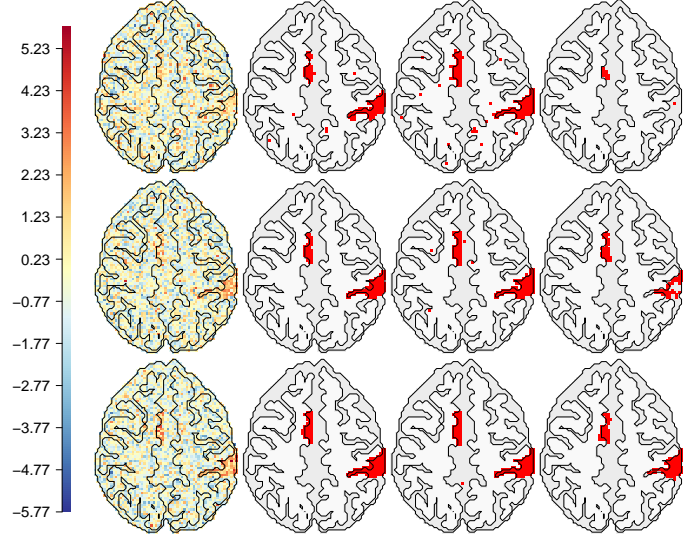


Fig. 4: Left-to-right: sample SPMs and best performers (AM-F_{0.05}, AR-F_{0.05} and AS) for experiments with CNR = 0.5 (top row), CNR = 0.75 (middle) and CNR = 1.0 (bottom). AR-F_{0.01} and AM-F_{0.01} out-performed AS but are not displayed.

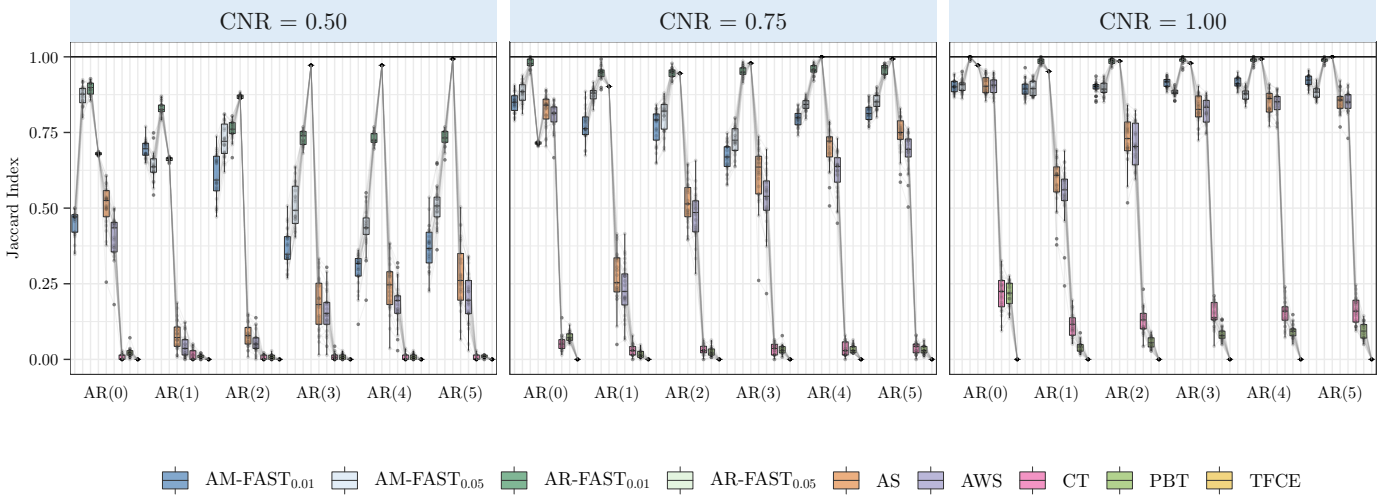


Fig. 5: Performance of the activation detection algorithms for different settings and when the AR coefficient decreases with order. For clarity, each setting displays performance of the methods in the same order as in the legend.

Our threshold α has a role, with smaller values performing better at higher CNRs and vice-versa. We suggest $\alpha \approx 0.01$ for high-CNR tasks and $\alpha \approx 0.05$ for tasks with low expected CNRs. One may use the upper percentile of the estimated voxel-wise CNRs to determine the low/high CNR scenario, with the upper percentile postulated so that an activated voxel (if such exists) is included in the CNR calculation. In our studies, AM-FAST required more Step 2 iterations, but was computationally slower than AR-FAST and had lower TPR, FPR and ω , especially at low CNRs. Regardless, both sets of FAST algorithms were the fastest among all methods.

C. Resting-State fMRI Dataset

A reviewer's suggestion led us to apply FAST on SPMs obtained upon fitting (1) to a resting state fMRI dataset [59], [60]. Both methods identified no activation even at $\alpha = 0.05$. This zero FPR (in a case with CNR=0) as opposed to the small FPR in low-CNR experiments may be due to Step 3 of our algorithm correctly allowing more Step 2 iterations to attenuate stray high-valued SPM voxels – termination is earlier in the low CNR cases given the spatially located weaker-signal peaks. For higher CNRs, Step 3 again adaptively admits more smoothing iterations that dampen stray high values in the SPM without substantially degrading the true high-signal peaks.

IV. ACTIVATION DURING PERCEPTION OF NOISY SPEECH

The dataset, provided as `data6` in the AFNI tutorial [54], is originally from an fMRI study [31] where a subject heard

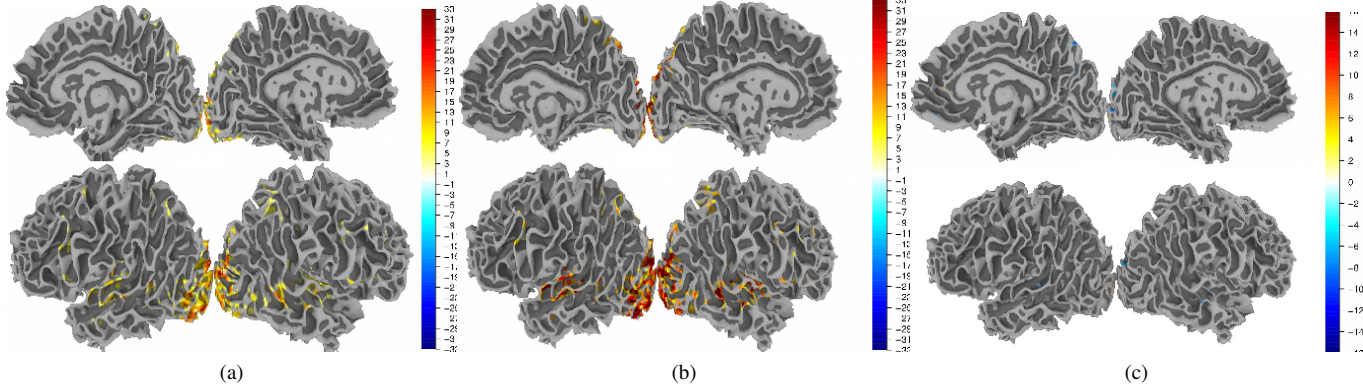


Fig. 6: AR-FAST-identified activation regions on SPMs obtained by fitting 1 with $AR(\hat{p})$ to AFNI's `data6` for (a) visual-reliable stimulus (b) audio-reliable stimulus and (c) the difference contrast between visual- and audio-reliable stimuli.

and saw a female speaker speak words, separately in audio-reliable and visual-reliable formats. In the first case, the subject clearly heard the spoken word but saw a degraded image of the speaker while in the visual-reliable case, the subject clearly saw the speaker vocalize the word but the audio was of reduced quality. There were three experimental runs, each consisting of a randomized design of 10 blocks, equally divided into blocks of audio-reliable and visual-reliable stimuli. T_2^* -weighted images with volumes of $80 \times 80 \times 33$ (with voxels of dimension $2.75 \times 2.75 \times 3.0 \text{ mm}^3$) from echo-planar sequences (TR=2s) were obtained over 152 time-points. Our interest was in determining activation corresponding to the audio ($H_0 : \beta_a = 0$) and visual ($H_0 : \beta_v = 0$) tasks, and also their contrast ($H_0 : \beta_v - \beta_a = 0$). The first two cases have one-sided alternatives while the contrast in activation corresponds to a two-sided alternative. At each voxel, we fitted AR models for $p = 0, 1, 2, 3, 4, 5$ and chose p with the highest BIC. Figure 6 uses AFNI and Surface Mapping (SUMA) to display activated regions obtained using AR-FAST on the SPM: corresponding maps for AM-FAST, AS, AWS and CT are in Figure S12. We used $\alpha = 0.01$ because the upper percentile of the voxel-wise estimated CNRs (all over 4) was high. Most of the activation occurs in Brodmann areas 18 and 19 (BA18 and BA19), which comprise the occipital cortex and the extrastriate (or peristriate) cortex. In humans with normal sight, the extrastriate cortex is an area for visual association, where feature-extraction, shape recognition, attentional and multimodal integrating functions occur. Increased activation was also observed in the superior temporal sulcus (STS), which recent studies [61] have shown is related to distinguishing voices from environmental sounds, stories versus nonsensical speech, moving faces versus moving objects, biological motion and so on. The other methods (including AM-FAST) also identify the same regions but they identify a lot more activated voxels, some of which appear to be false positives. Although a detailed analysis of the results of this study is beyond the purview of this paper, we note that AR-FAST finds interpretable results even when applied to a single subject high-level cognition experiment.

V. DISCUSSION

In this paper, we have proposed a new fully automated and adaptive smoothing and thresholding algorithm called FAST with the ability to perform activation detection in low-signal settings. Two variants, AM-FAST and AR-FAST, are proposed with the latter slightly recommended over the former. Our methodology realistically accounts for both spatial correlation structure and uses more accurate extreme value theory in its development. Experiments indicate good performance over a range of low-CNR settings and real datasets. Our method is implemented by a publicly available R package `RFASTFMRI` and is fully automated with one threshold choice for which we provide the user with easily-implemented guidance. This contrasts with AS and AWS where the user has to set a maximum smoothing bandwidth related to the expected diameter of activated regions [41] – a determination that in our view requires considerable dexterity and is ambivalent when different-sized regions are expected to be activated.

A reviewer has pointed us to the joint detection-estimation literature [62], [63] where estimation of the HRF and activation detection occur jointly. The FAST, AS and AWS algorithms can be placed in a related framework, with the difference that the estimation step is of a more spatially consistent (smoothed) SPM. We also agree with another reviewer on other ways of ensuring spatial contiguity such as through Markov Random Field priors [64] and on the need to incorporate approaches that also allow for nonhomogeneous smoothing. Developing FAST for more sophisticated time series and spatial models, including in the context of complex fMRI [65] as well as increased use of diagnostics in understanding activation and cognition are important research areas and directions that would benefit from further attention.

ACKNOWLEDGMENT

The authors sincerely thank four anonymous reviewers and an Associate Editor whose helpful and insightful comments on an earlier version of this article greatly improved its content.

REFERENCES

- [1] J. W. Belliveau, D. N. Kennedy, R. C. McKinstry, B. R. Buchbinder, R. M. Weisskoff, M. S. Cohen, J. M. Vevea, T. J. Brady, and B. R. Rosen, "Functional mapping of the human visual cortex by magnetic resonance imaging," *Science*, vol. 254, pp. 716–719, 1991.
- [2] K. K. Kwong, J. W. Belliveau, D. A. Chesler, I. E. Goldberg, R. M. Weisskoff, B. P. Poncelet, D. N. Kennedy, B. E. Hoppel, M. S. Cohen, R. Turner, H.-M. Cheng, T. J. Brady, and B. R. Rosen, "Dynamic magnetic resonance imaging of human brain activity during primary sensory stimulation," *Proceedings of the National Academy of Sciences of the United States of America*, vol. 89, pp. 5675–5679, 1992.
- [3] P. A. Bandettini, A. Jesmanowicz, E. C. Wong, and J. S. Hyde, "Processing strategies for time-course data sets in functional MRI of the human brain," *Magnetic Resonance in Medicine*, vol. 30, pp. 161–173, 1993.
- [4] K. J. Friston, A. P. Holmes, K. J. Worsley, J.-B. Poline, C. D. Frith, and R. S. J. Frackowiak, "Statistical parametric maps in functional imaging: A general linear approach," *Human Brain Mapping*, vol. 2, pp. 189–210, 1995.
- [5] A. M. Howseman and R. W. Bowtell, "Functional magnetic resonance imaging: imaging techniques and contrast mechanisms," *Philosophical Transactional of the Royal Society, London*, vol. 354, pp. 1179–94, 1999.
- [6] W. D. Penny, K. J. Friston, J. T. Ashburner, S. J. Kiebel, and T. E. Nichols, Eds., *Statistical Parametric Mapping: The Analysis of Functional Brain Images*, 1st ed. Academic Press, 2006.
- [7] M. A. Lindquist, "The statistical analysis of fMRI data," *Statistical Science*, vol. 23, no. 4, pp. 439–464, 2008.
- [8] N. A. Lazar, *The Statistical Analysis of Functional MRI Data*. Springer, 2008.
- [9] F. G. Ashby, *Statistical Analysis of fMRI Data*. MIT Press, 2011.
- [10] S. Ogawa, T. M. Lee, A. S. Nayak, and P. Glynn, "Oxygenation-sensitive contrast in magnetic resonance image of rodent brain at high magnetic fields," *Magnetic Resonance in Medicine*, vol. 14, pp. 68–78, 1990.
- [11] S. Ogawa, T. M. Lee, A. R. Kay, and D. W. Tank, "Brain magnetic resonance imaging with contrast dependent on blood oxygenation," *Proceedings of the National Academy of Sciences, USA*, vol. 87, no. 24, pp. 9868–9872, 1990.
- [12] K. J. Worsley, C. H. Liao, J. Aston, V. Petre, G. H. Duncan, F. Morales, and A. C. Evans, "A general statistical analysis for fmri data," *NeuroImage*, vol. 15, pp. 1–15, 2002.
- [13] K. J. Friston, P. Fletcher, O. Josephs, A. Holmes, M. Rugg, and R. Turner, "Event-related fMRI: characterizing differential responses," *Neuroimage*, vol. 7, no. 1, pp. 30–40, 1998.
- [14] G. H. Glover, "Deconvolution of impulse response in event-related bold fmri," *NeuroImage*, vol. 9, pp. 416–429, 1999.
- [15] R. B. Buxton, K. Uludağ, D. J. Dubowitz, and T. T. Liu, "Modeling the hemodynamic response to brain activation," *Neuroimage*, vol. 23, pp. S220–S233, 2004.
- [16] K. J. Friston, C. D. Frith, P. F. Liddle, R. J. Dolan, A. A. Lammertsma, and R. S. J. Frackowiak, "The relationship between global and local changes in PET scans," *Journal of Cerebral Blood Flow and Metabolism*, vol. 10, pp. 458–466, 1990.
- [17] K. J. Friston, A. P. Holmes, K. J. Worsley, J.-P. Poline, C. D. Frith, and R. S. J. Frackowiak, "Statistical parametric maps in functional imaging: a general linear approach," *Human brain mapping*, vol. 2, no. 4, pp. 189–210, 1994.
- [18] K. J. Worsley and K. J. Friston, "Analysis of fMRI time-series revisited again," *Neuroimage*, vol. 2, no. 3, pp. 173–181, 1995.
- [19] C. R. Genovese, N. A. Lazar, and T. Nichols, "Thresholding of statistical maps in functional neuroimaging using the false discovery rate," *Neuroimage*, vol. 15, pp. 870–878, 2002.
- [20] J. V. Hajnal, R. Myers, A. Oatridge, J. E. Schweiso, J. R. Young, and G. M. Bydder, "Artifacts due to stimulus-correlated motion in functional imaging of the brain," *Magnetic Resonance in Medicine*, vol. 31, pp. 283–291, 1994.
- [21] B. Biswal, A. E. DeYoe, and J. S. Hyde, "Reduction of physiological fluctuations in fMRI using digital filters," *Magnetic Resonance in Medicine*, vol. 35, no. 1, pp. 107–113, January 1996. [Online]. Available: <http://view.ncbi.nlm.nih.gov/pubmed/8771028>
- [22] R. P. Wood, S. T. Grafton, J. D. G. Watson, N. L. Sicotte, and J. C. Mazziotta, "Automated image registration. ii. intersubject validation of linear and non-linear models," *Journal of Computed Assisted Tomography*, vol. 22, pp. 253–265, 1998.
- [23] R. P. Gullapalli, R. Maitra, S. Roys, G. Smith, G. Alon, and J. Greenspan, "Reliability estimation of grouped functional imaging data using penalized maximum likelihood," *Magnetic Resonance in Medicine*, vol. 53, pp. 1126–1134, 2005.
- [24] R. Maitra, S. R. Roys, and R. P. Gullapalli, "Test-retest reliability estimation of functional mri data," *Magnetic Resonance in Medicine*, vol. 48, pp. 62–70, 2002.
- [25] R. Maitra, "Initializing partition-optimization algorithms," *IEEE/ACM Transactions on Computational Biology and Bioinformatics*, vol. 6, pp. 144–157, 2009. [Online]. Available: <http://doi.ieeecomputersociety.org/10.1109/TCBB.2007.70244>
- [26] Z. S. Saad, D. R. Glen, G. Chen, M. S. Beauchamp, R. Desai, and R. W. Cox, "A new method for improving functional-to-structural mri alignment using local pearson correlation," *NeuroImage*, vol. 44, pp. 839–848, 2009.
- [27] E. E. Chen and S. L. Small, "Test-retest reliability in fMRI of language: Group and task effects," *Brain and Language*, vol. 102, no. 2, pp. 176–85, 2007. [Online]. Available: <http://dx.doi.org/10.1016/j.bandl.2006.04.015>
- [28] K. D. Kryter, *The handbook of hearing and the effects of noise: Physiology, psychology, and public health*. Academic Press, 1994.
- [29] M. D. Hauser, *The evolution of communication*. MIT press, 1996.
- [30] S. Dupont and J. Luettin, "Audio-visual speech modeling for continuous speech recognition," *IEEE Transactions on Multimedia*, vol. 2, no. 3, pp. 141–151, 2000.
- [31] A. R. Nath and M. S. Beauchamp, "Dynamic changes in superior temporal sulcus connectivity during perception of noisy audiovisual speech," *The Journal of Neuroscience*, vol. 31, no. 5, p. 1704 1714, 2011.
- [32] W. H. Sumby and I. Pollack, "Visual contribution to speech intelligibility in noise," *The Journal of the Acoustical Society of America*, vol. 26, no. 2, pp. 212–215, 1954.
- [33] B. E. Stein and M. A. Meredith, *The merging of the senses*. The MIT Press, 1993.
- [34] Y. Benjamini, A. M. Krieger, and D. Yekutieli, "Adaptive linear step-up procedures that control the false discovery rate," *Biometrika*, vol. 93, no. 3, pp. 491–507, 2006.
- [35] R. Heller, D. Stanley, D. Yekutieli, N. Rubin, and Y. Benjamini, "Cluster-based analysis of fMRI data," *NeuroImage*, vol. 33, no. 2, pp. 599–608, Nov. 2006. [Online]. Available: <http://dx.doi.org/10.1016/j.neuroimage.2006.04.233>
- [36] Y. Benjamini and R. Heller, "False discovery rates for spatial signals," *Journal of the American Statistical Association*, vol. 102, no. 480, pp. 1272–1281, 2007.
- [37] M. Smith and L. Fahrmeir, "Spatial Bayesian variable selection with application to functional Magnetic Resonance Imaging," *Journal of the American Statistical Association*, vol. 102, no. 478, pp. 417–431, 2007. [Online]. Available: <http://pubs.amstat.org/doi/abs/10.1198/016214506000001031>
- [38] S. M. Smith and T. E. Nichols, "Threshold-free cluster enhancement: Addressing problems of smoothing, threshold dependence and localisation in cluster inference," *Neuroimage*, vol. 44, pp. 83–98, 2009.

[39] C.-W. Woo, A. Krishnan, and T. D. Wager, "Cluster-extent based thresholding in fMRI analyses: Pitfalls and recommendations," *Neuroimage*, vol. 91, p. 412419, 2014.

[40] K. Tabelow, J. Polzehl, H. U. Voss, and V. Spokoiny, "Analyzing fMRI experiments with structural adaptive smoothing procedures," *NeuroImage*, vol. 33, no. 1, pp. 55–62, 2006.

[41] J. Polzehl, H. U. Voss, and K. Tabelow, "Structural adaptive segmentation for statistical parametric mapping," *NeuroImage*, vol. 52, no. 2, pp. 515–523, 2010.

[42] M. M. Monti, "Statistical analysis of fMRI time-series: A critical review of the glm approach," *Frontiers in Human Neuroscience*, vol. 5, no. 00028, pp. 1–13, 2011. [Online]. Available: http://www.frontiersin.org/Journal/Abstract.aspx?s=537&name=human_neuroscience&ART_DOI=10.3389/fnhum.2011.00028

[43] W.-L. Luo and T. E. Nichols, "Diagnosis and exploration of massively univariate neuroimaging models," *Neuroimage*, vol. 19, no. 3, pp. 1014–1032, 2003.

[44] J. M. Loh, M. A. Lindquist, and T. D. Wager, "Residual analysis for detecting mis-modeling in fMRI," *Statistica Sinica*, pp. 1421–1448, 2008.

[45] M. Lindquist, J. Loh, L. Atlas, and T. Wager, "Modeling the hemodynamic response function in fMRI: Efficiency, bias and mis-modeling," *Neuroimage*, vol. 45, no. 1, p. S187S196, 2009.

[46] G. Schwarz, "Estimating the dimensions of a model," *Annals of Statistics*, vol. 6, pp. 461–464, 1978.

[47] R. H. Shumway and D. S. Stoffer, *Time Series Analysis and Its Applications*, 2nd ed. Springer, 2006.

[48] S. I. Resnick, *Extreme values, regular variation and point processes*. Springer, 2013.

[49] H. A. David and H. N. Nagaraja, *Order Statistics*. Hoboken, New Jersey: John Wiley and Sons, Inc., 2003.

[50] R. Von Mises, "La distribution de la plus grande de n valeurs," *Rev. math. Union interbalcanique*, vol. 1, no. 1, 1936.

[51] D. Garcia, "Robust smoothing of gridded data in one and higher dimensions with missing values," *Computational statistics & data analysis*, vol. 54, no. 4, pp. 1167–1178, 2010.

[52] P. Jaccard, "Étude comparative de la distribution florale dans une portion des alpes et des jura," *Bulletin de la Société Vaudoise des Sciences Naturelles*, vol. 37, p. 547579, 1901.

[53] R. Maitra, "A re-defined and generalized percent-overlap-of-activation measure for studies of fMRI reproducibility and its use in identifying outlier activation maps," *Neuroimage*, vol. 50, no. 1, pp. 124–135, 2010.

[54] R. W. Cox, "AFNI: software for analysis and visualization of functional magnetic resonance neuroimages," *Computers and Biomedical research*, vol. 29, no. 3, pp. 162–173, 1996.

[55] A. M. Winkler, G. R. Ridgway, M. A. Webster, S. M. Smith, and T. E. Nichols, "Permutation inference for the general linear model," *Neuroimage*, vol. 92, pp. 381–397, 2014.

[56] J. Polzehl and V. Spokoiny, "Propagation-separation approach for local likelihood estimation," *Probability Theory and Related Fields*, vol. 135, no. 3, pp. 335–362, 2006.

[57] R. Maitra, "Assessing certainty of activation or inactivation in test-retest fMRI studies," *Neuroimage*, vol. 47, no. 1, pp. 88–97, 2009.

[58] E. J. Hoffman, P. D. Cutler, W. M. Digby, and J. C. Mazziotta, "3-d phantom to simulate cerebral blood flow and metabolic images for pet," *IEEE Transactions on Nuclear Science*, vol. 37, pp. 616–620, 1990.

[59] A. D. Barber, P. Srinivasan, S. E. Joel, B. S. Caffo, J. J. Pekar, and S. H. Mostofsky, "Motor dexterity?: evidence that left hemisphere lateralization of motor circuit connectivity is associated with better motor performance in children," *Cerebral Cortex*, vol. 22, no. 1, pp. 51–59, 2011.

[60] M. B. Nebel, S. E. Joel, J. Muschelli, A. D. Barber, B. S. Caffo, J. J. Pekar, and S. H. Mostofsky, "Disruption of functional organization within the primary motor cortex in children with autism," *Human brain mapping*, vol. 35, no. 2, pp. 567–580, 2014.

[61] E. Grossman and R. Blake, "Brain activity evoked by inverted and imagined biological motion," *Vision research*, vol. 41, no. 10, pp. 1475–1482, 2001.

[62] S. Makni, P. Ciuciu, J. Idier, and J.-B. Poline, "Joint detection-estimation of brain activity in functional MRI: a multichannel deconvolution solution," *IEEE Transactions on Signal Processing*, vol. 53, no. 9, pp. 3488–3502, 2005.

[63] ———, "Joint detection-estimation of brain activity in fMRI using an autoregressive noise model," in *Biomedical Imaging: Nano to Macro, 2006. 3rd IEEE International Symposium on*. IEEE, 2006, pp. 1048–1051.

[64] B. Ng, G. Hamarneh, and R. Abugharbieh, "Modeling brain activation in fMRI using group MRF," *IEEE Transactions on Medical Imaging*, vol. 31, no. 5, pp. 1113–1123, 2012.

[65] D. W. Adrian, R. Maitra, and D. B. Rowe, "Complex-valued time series modeling for improved activation detection in fMRI studies," *Annals of Applied Statistics*, vol. 12, no. 3, pp. 1451–1478, 2018.

SUPPLEMENTARY MATERIALS

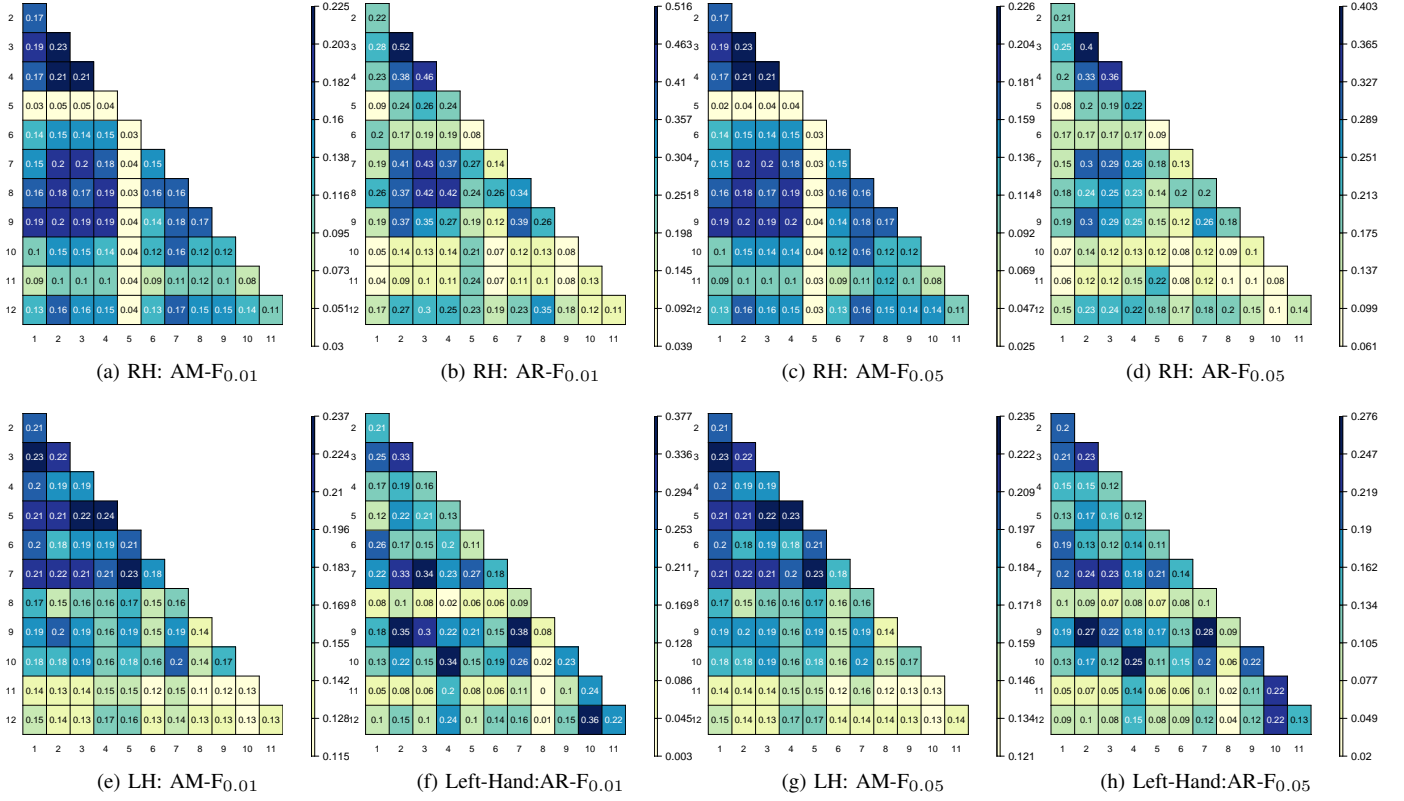


Fig. S1: Pairwise Jaccard Indices for the activation maps using AM- and AR-FAST for the replications of the right-hand (top panel) and left-hand (bottom panel) finger-tapping experiments.

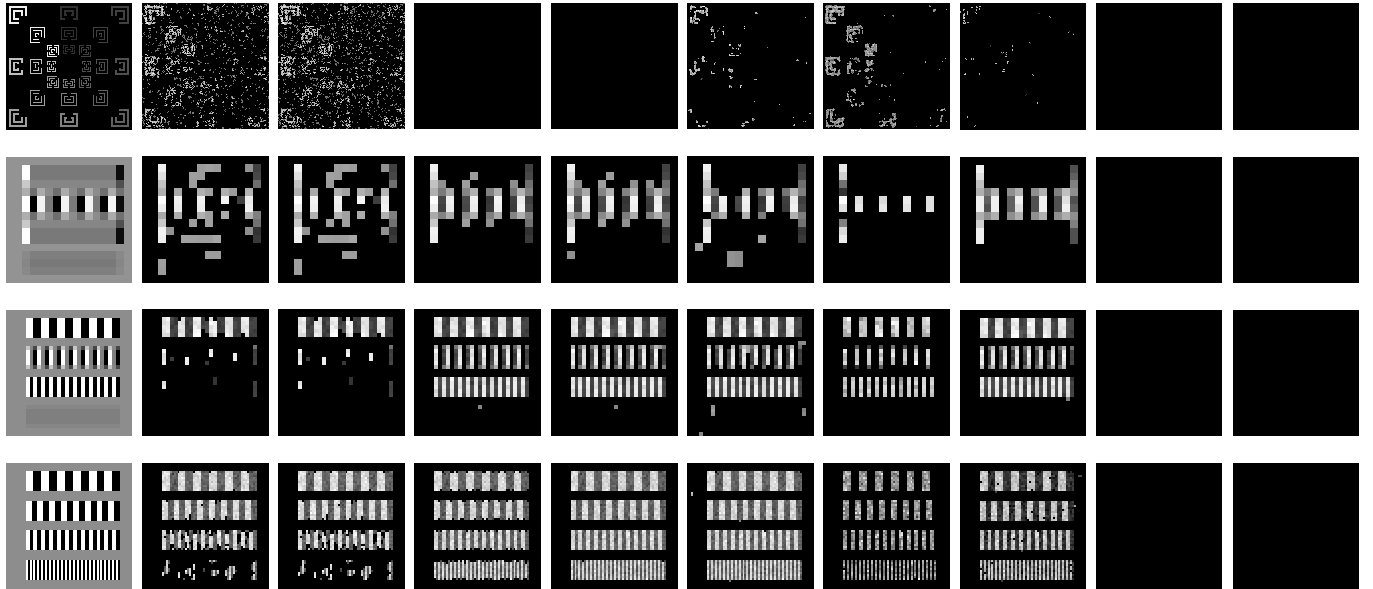


Fig. S2: True and activated voxels in the SPM upon using AM-FAST with $\alpha = 0.01$ and 0.05 , AR-FAST with $\alpha = 0.01$ and 0.05 , AS, AWS, CT, PBT and TFCE for the Motif (top row) and the 16×16 , 32×32 and 64×64 stripes (last three rows).

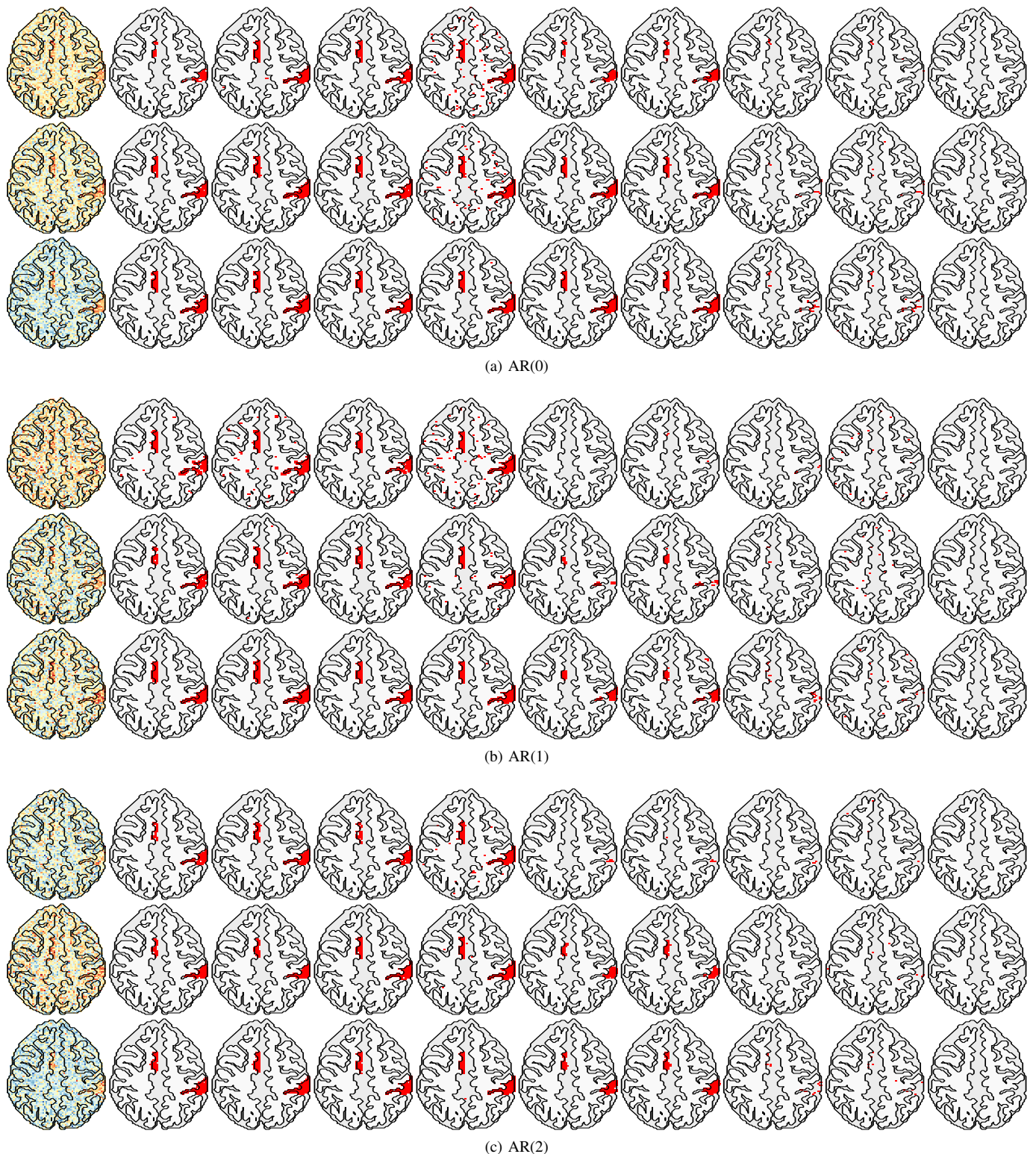
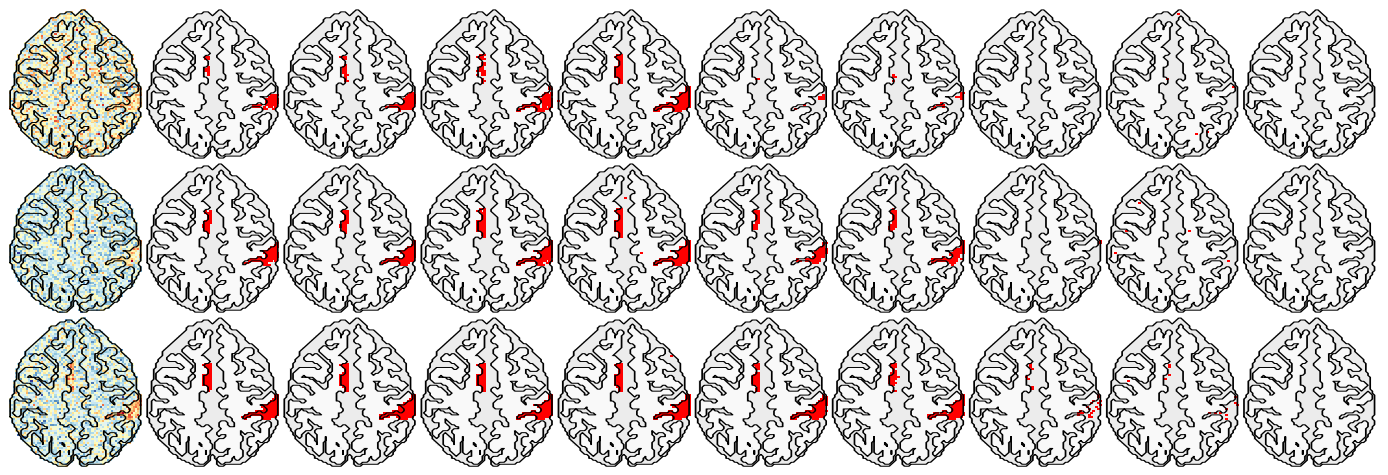
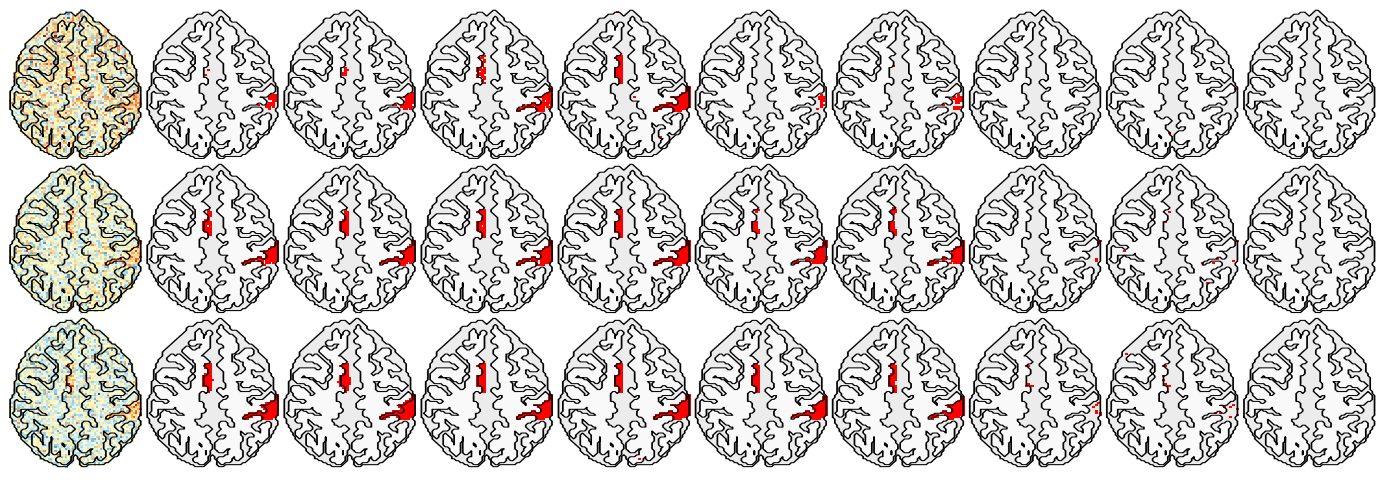


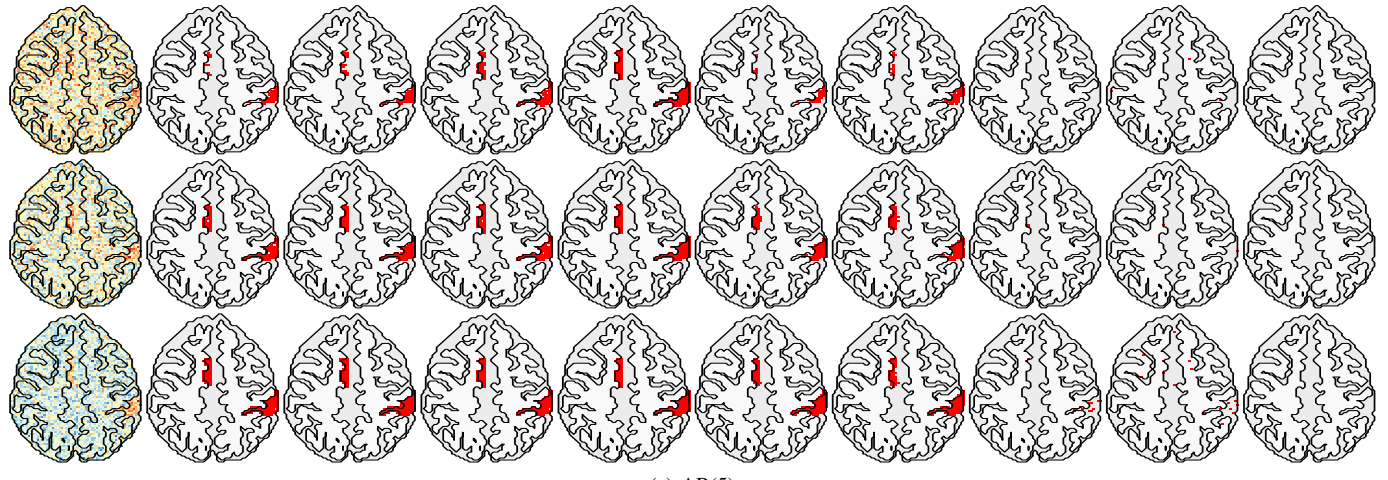
Fig. S3: Sample SPMs (left column) and corresponding activation maps from the modified Hoffman phantom obtained for CNR = 0.5 (top), 0.75 (middle) and 1.0 (bottom) using (from left to right) AM-FAST with $\alpha = 0.01$ and $\alpha = 0.05$, AR-FAST with $\alpha = 0.01$ and $\alpha = 0.05$, AS, AWS, CT, PBT and TFCE for AR(p) errors with (a) $p = 0$, (b) $p = 1$ and (c) $p = 2$ with AR coefficients decreasing with autocorrelation order.



(a) AR(3)

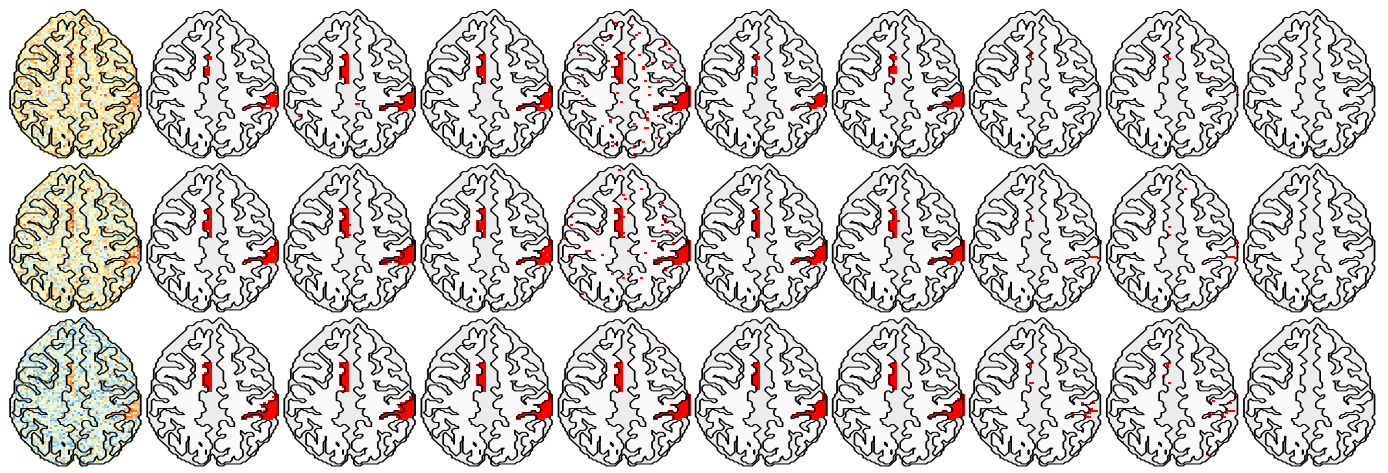


(b) AR(4)

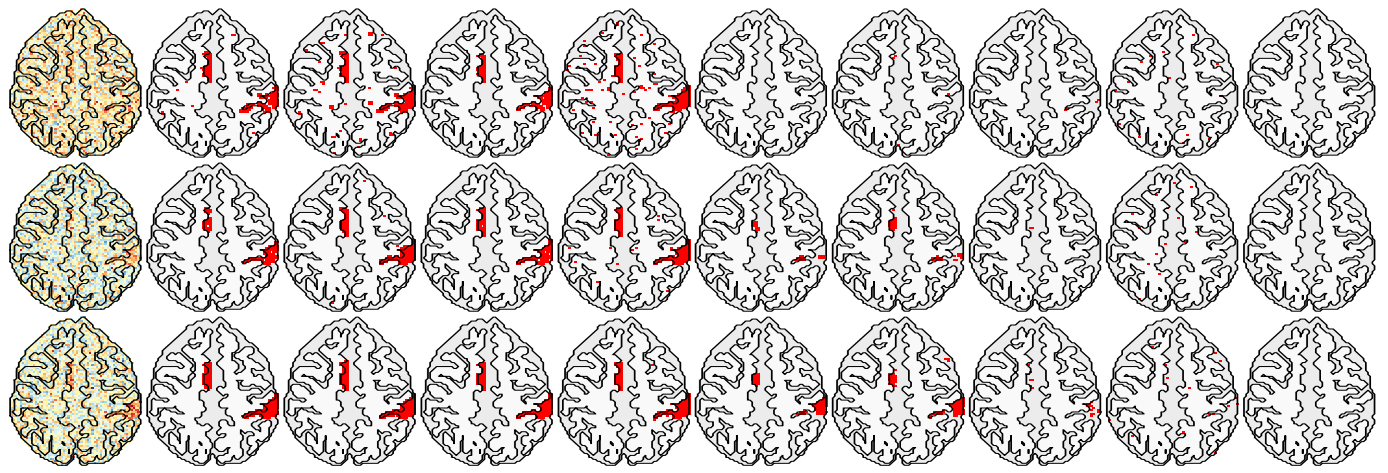


(c) AR(5)

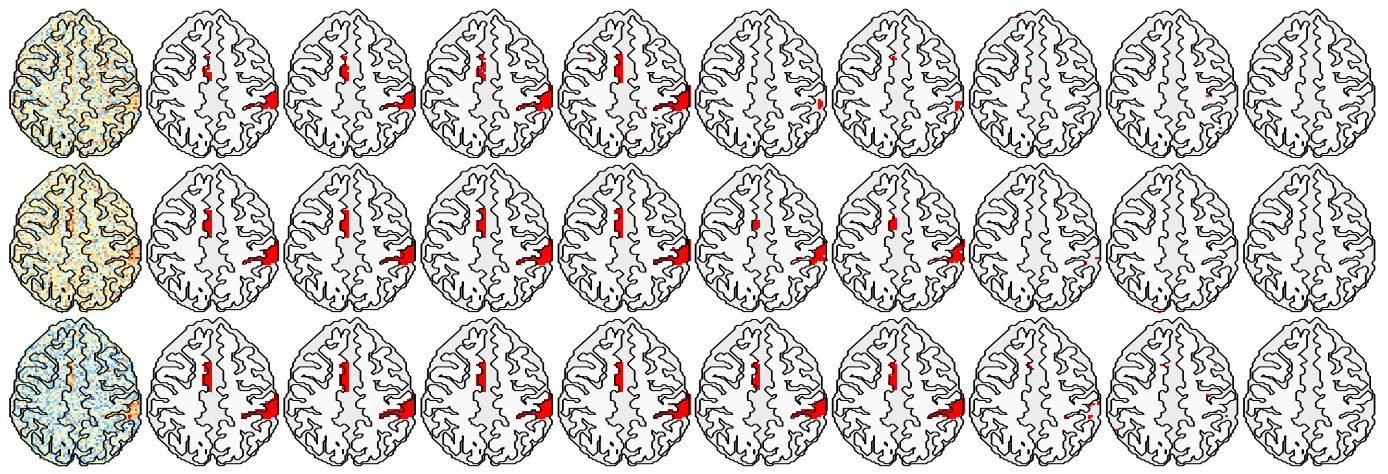
Fig. S4: SPMs and corresponding activation maps in a similar framework as Figure S3, but for p : we have (a) $p = 3$, (b) $p = 4$ and (c) $p = 5$.



(a) AR(0)

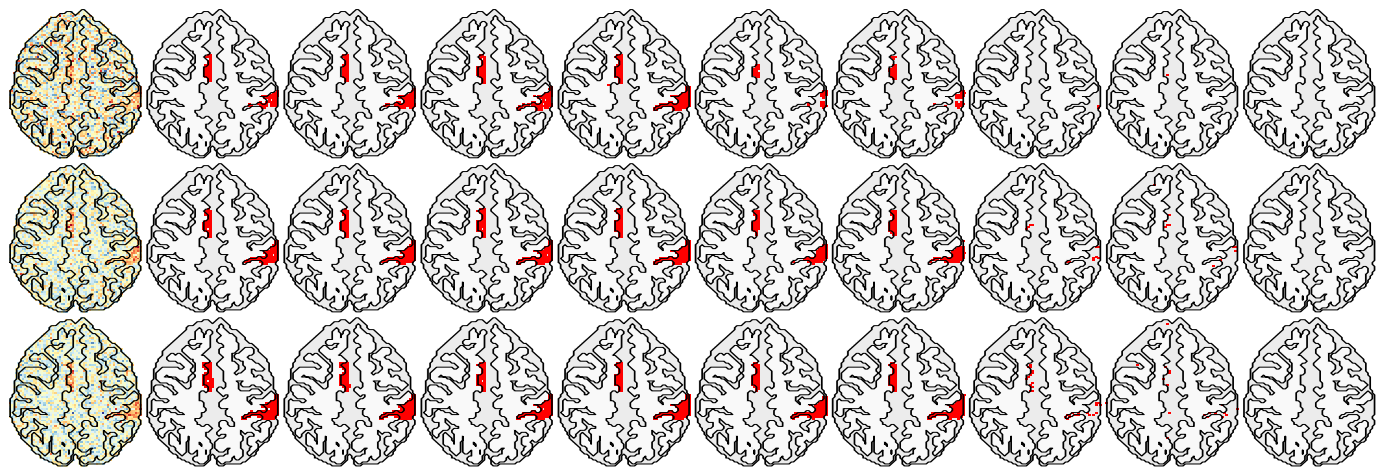


(b) AR(1)

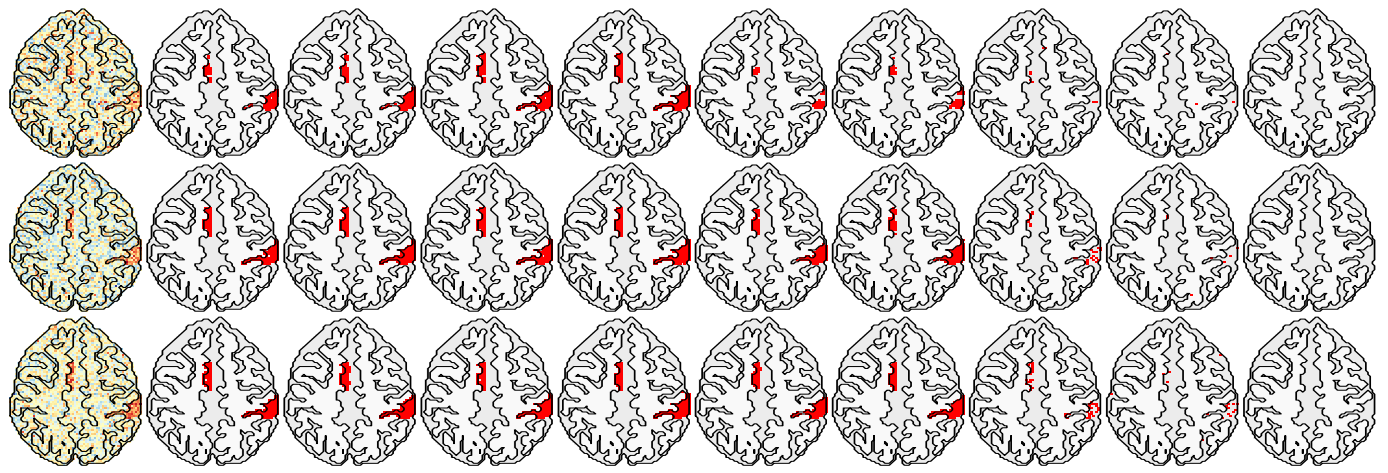


(c) AR(2)

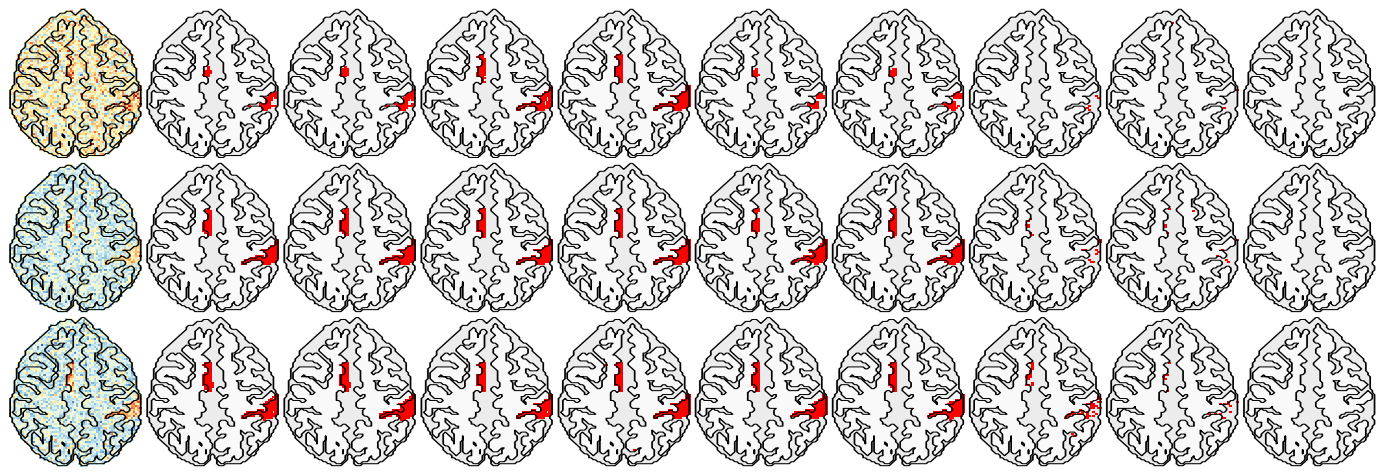
Fig. S5: Sample SPMs and corresponding activation maps in a similar framework as Figure S3, but here the AR coefficients are in increasing order



(a) AR(3)



(b) AR(4)



(c) AR(5)

Fig. S6: Sample SPMs and corresponding activation maps in a similar framework as Figure S4, but here the AR coefficients are in increasing order

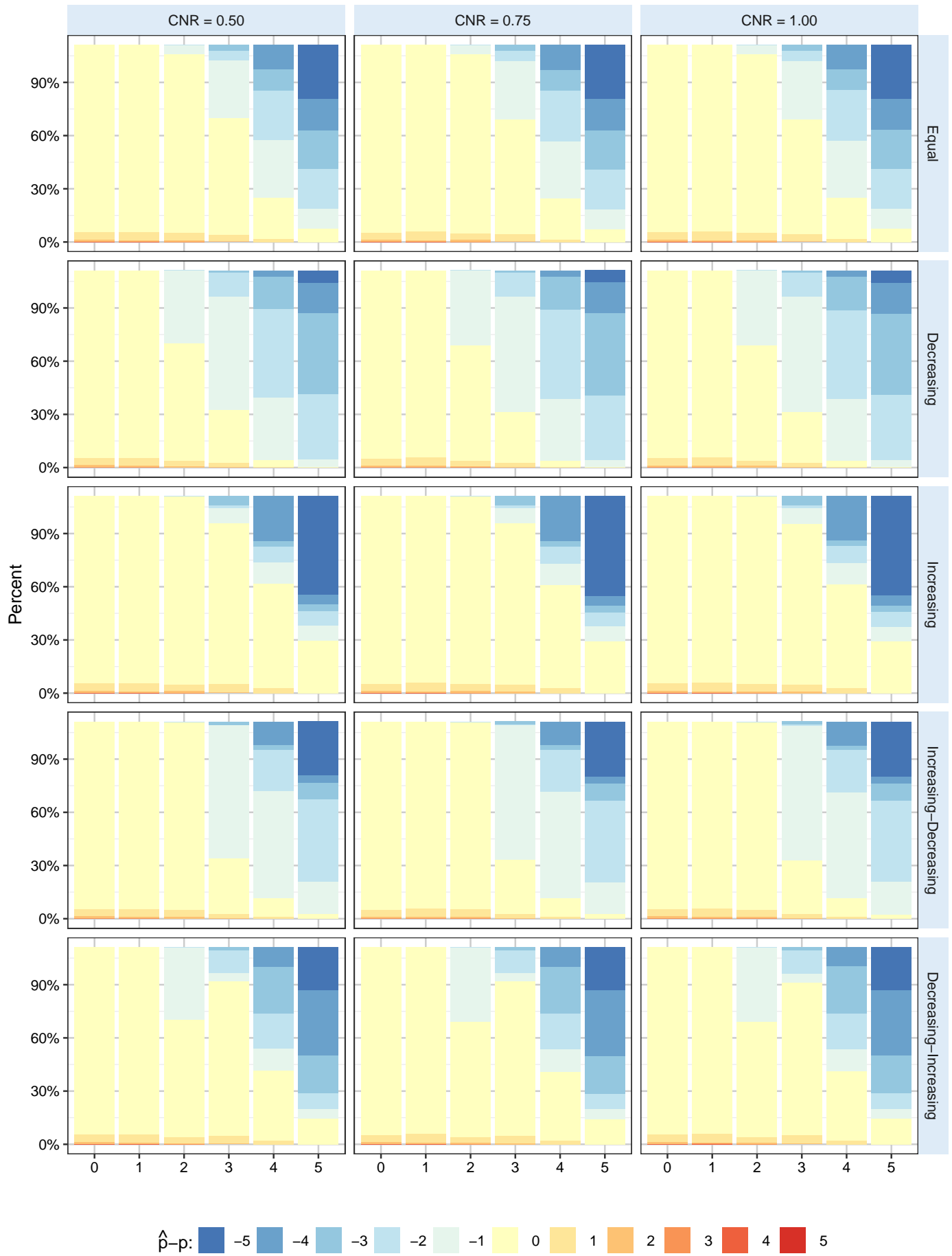


Fig. S7: Distribution of the difference in estimated and true orders for the large-scale simulation study of Section III-B2.

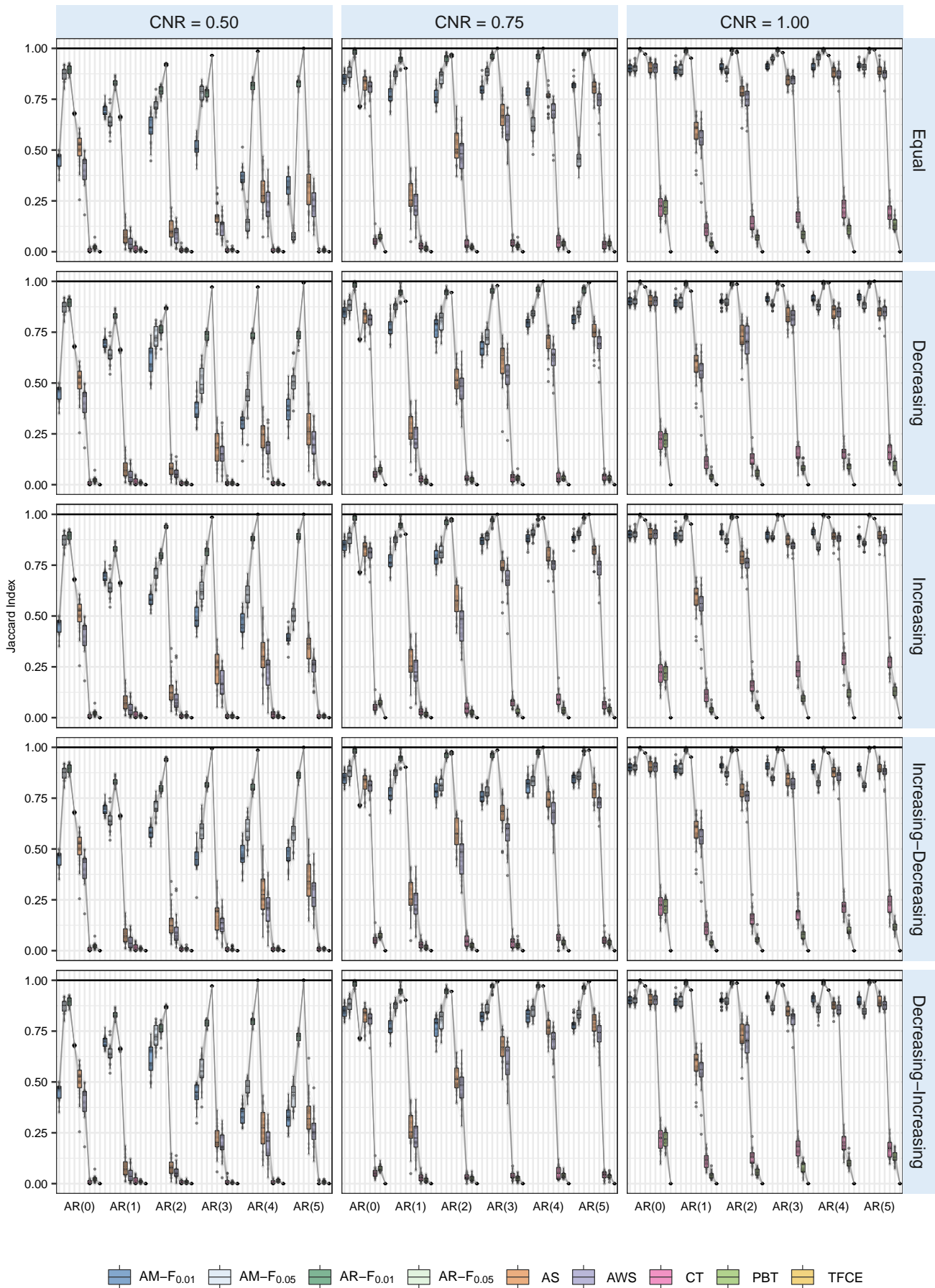


Fig. S8: Performance, in terms of the Jaccard Index, for each of the algorithms for the different experimental setup and settings. As in Figure 5, each method is displayed for each setting in the boxplot in the same order as in the legend.

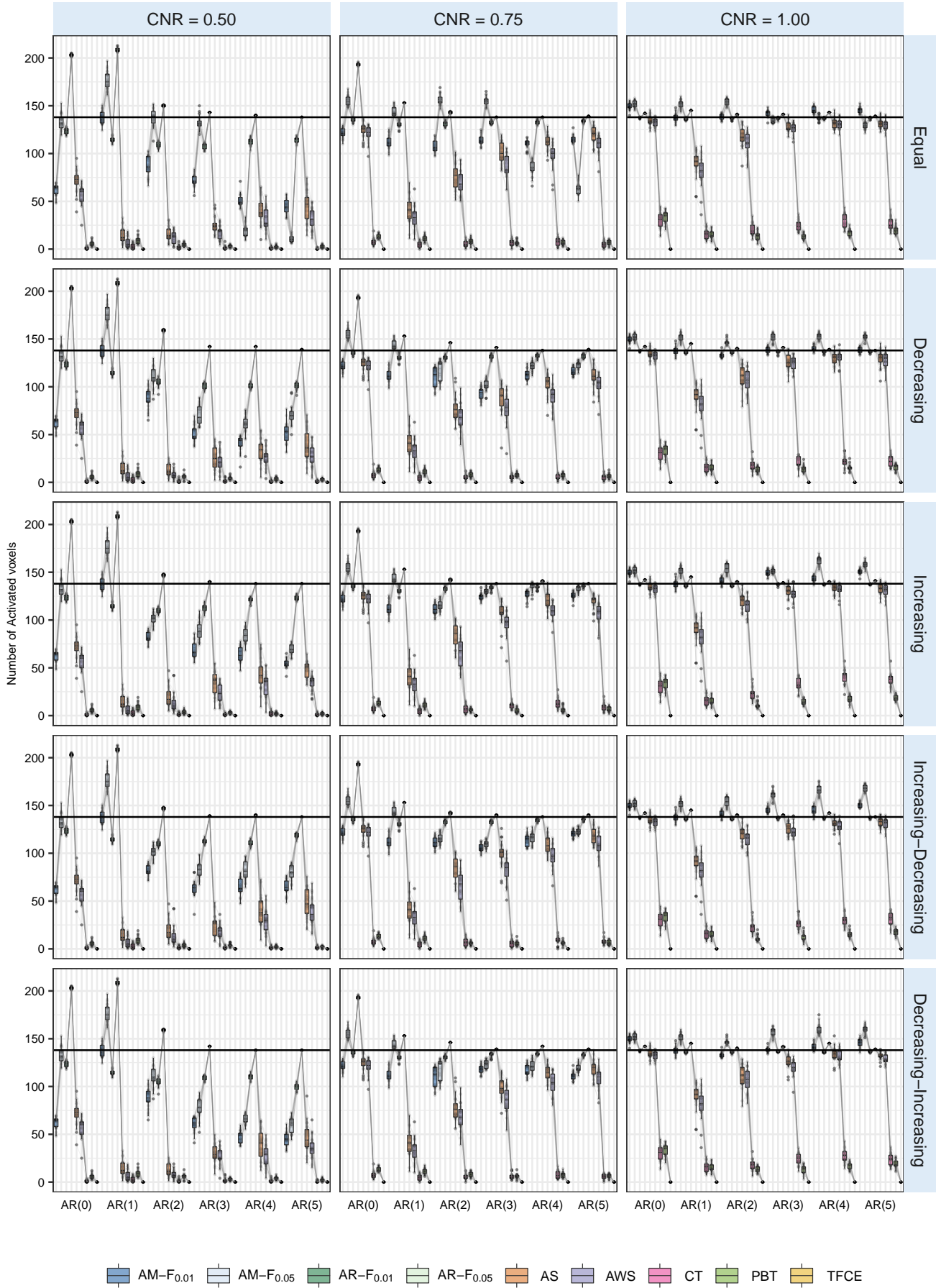


Fig. S9: Number of activated voxels in activation maps obtained with the modified Hoffman phantom and the AM-FAST, AR-FAST, AS, AWS, CT, PBT and TFCE algorithms for the different simulation settings. The horizontal line shows the number of truly active voxels.

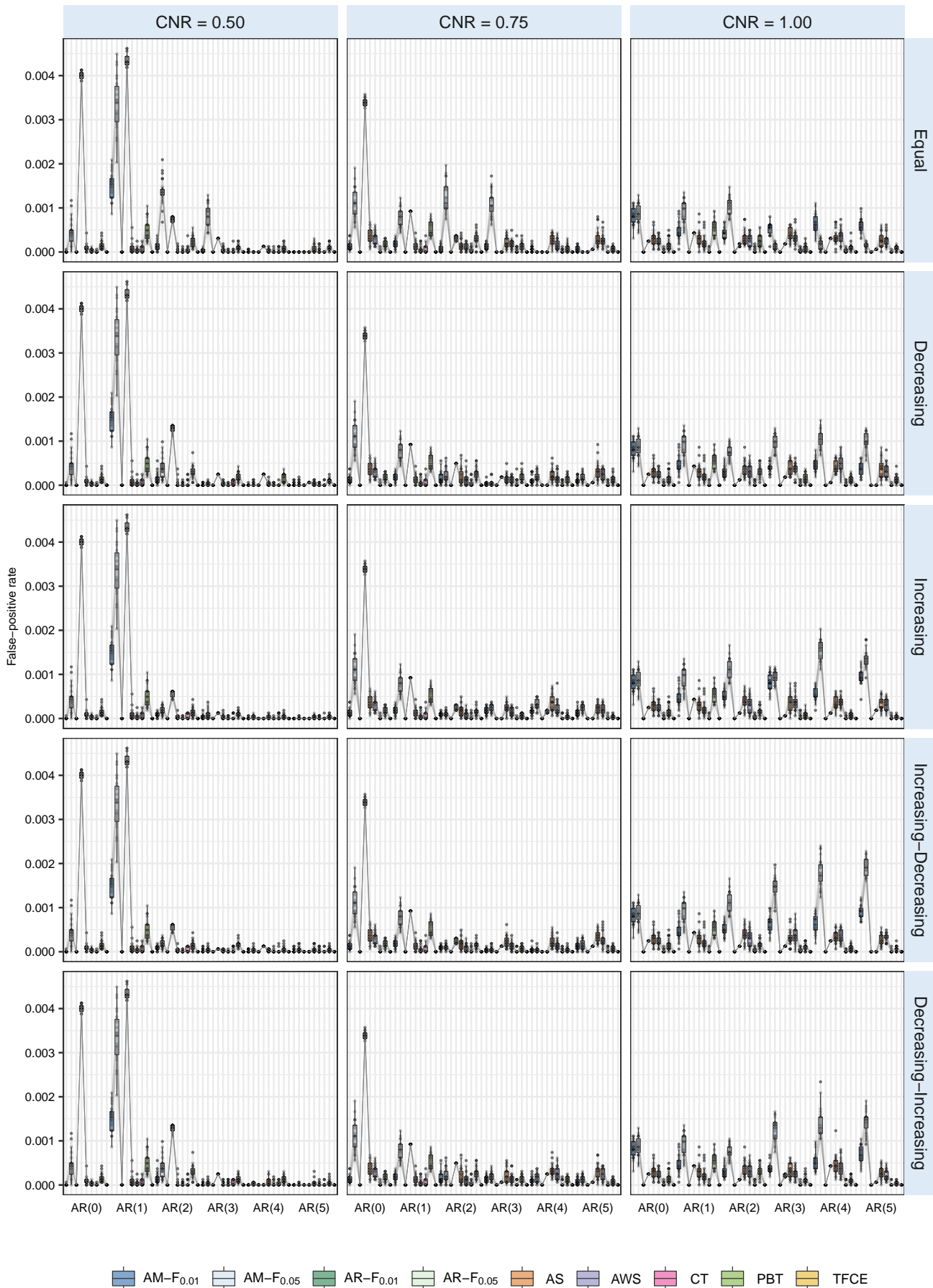


Fig. S10: False Positive Rate of the AM-FAST, AR-FAST, AS, AWS, CT, PBT and TFCE algorithms using the modified Hoffman phantom and for the different simulation settings.

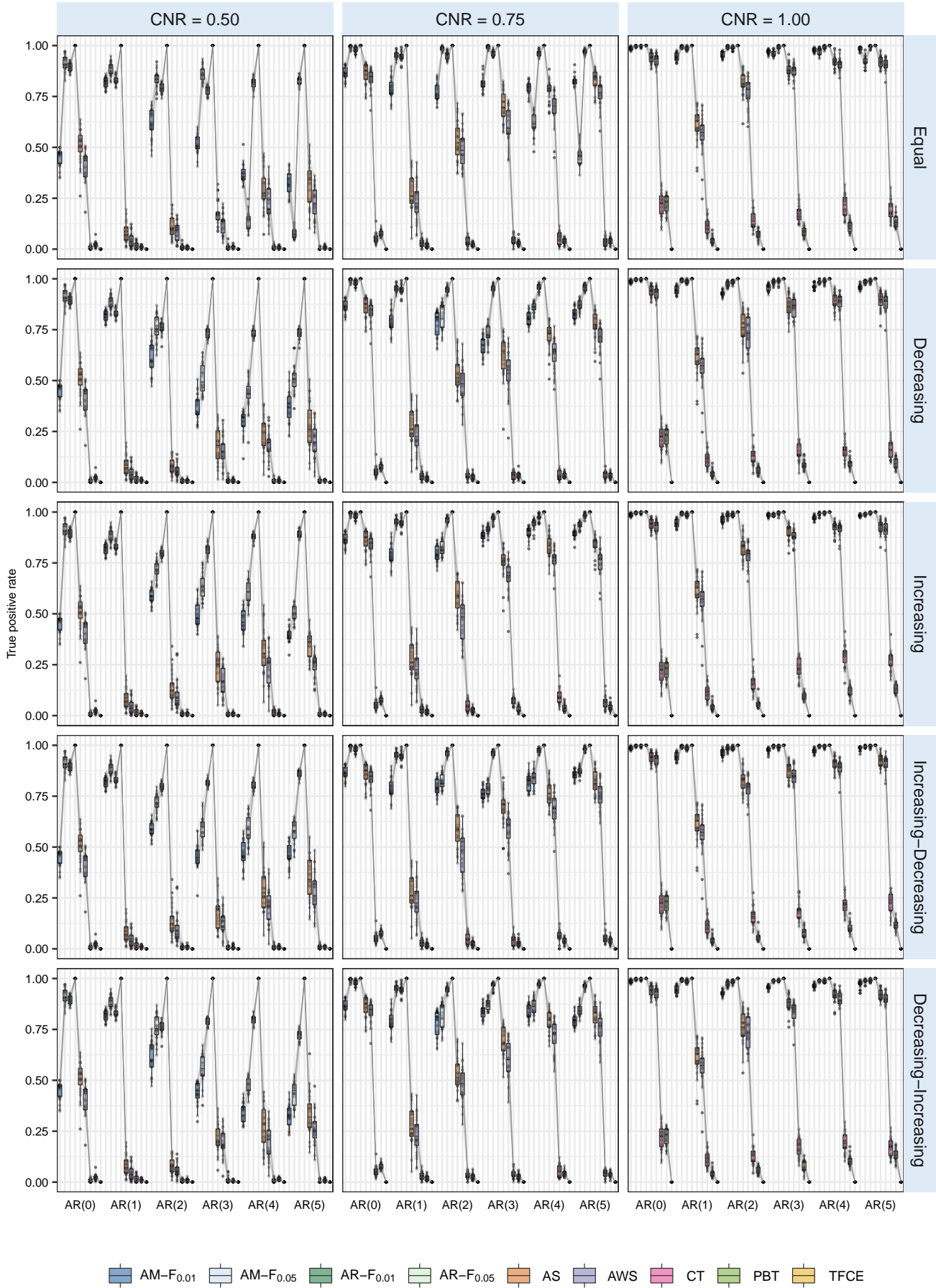


Fig. S11: True Positive Rate of the AM-FAST, AR-FAST, AS, AWS, CT, PBT and TFCE algorithms for the different simulation settings using the modified Hoffman phantom.

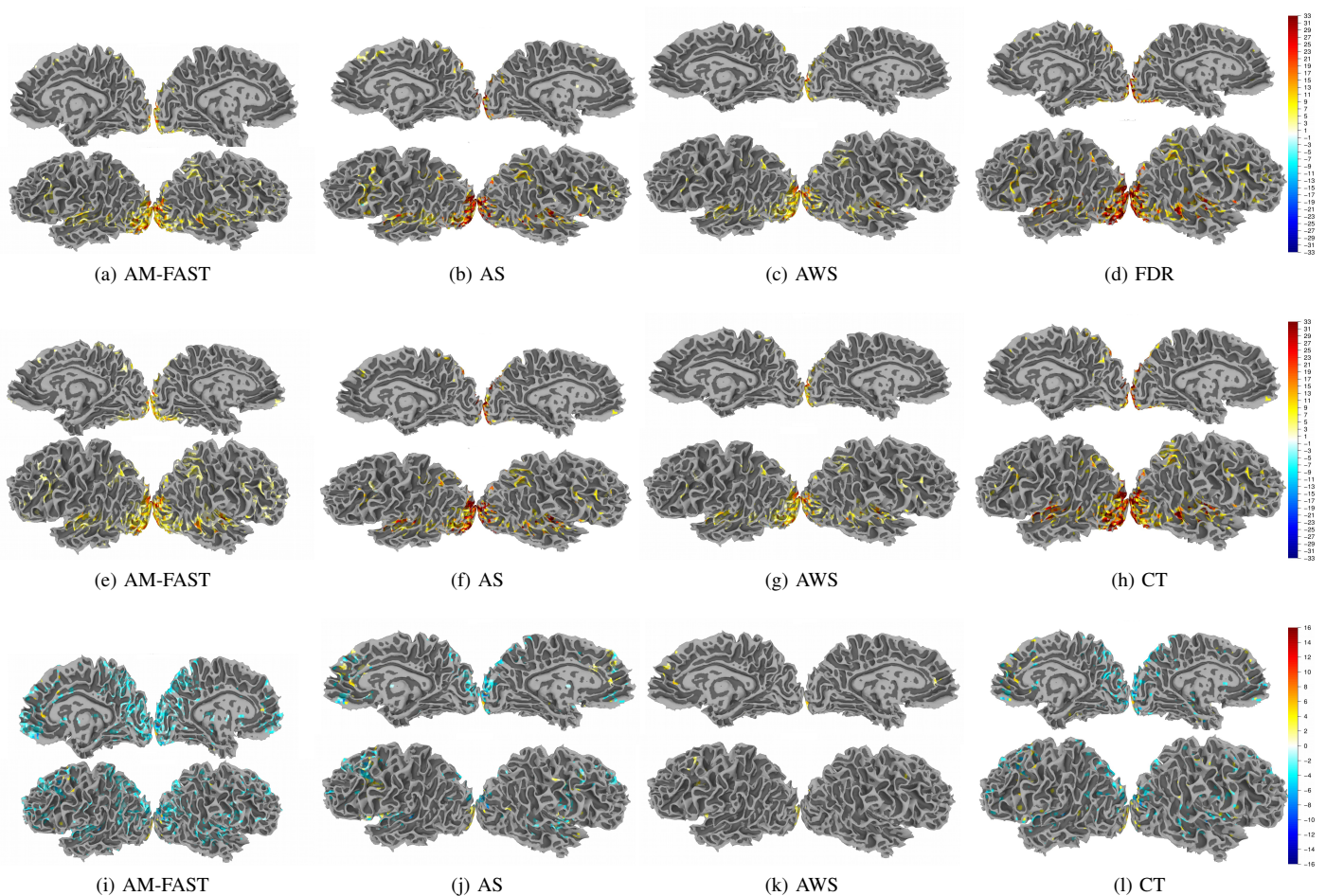


Fig. S12: Activation regions in *AFNI data6* obtained using AM-FAST, AS, AWS, and CT on SPMs upon fitting $AR(\hat{\rho})$ on 1. The first row is for the visual-reliable stimulus, the second row is for audio-reliable stimulus and third row is for the difference contrast between visual- and audio-reliable stimuli.